DEVELOPMENT OF MECHANICAL DRIVEN

DNA NANOMOTORS

LOH IONG YING

(M.Sc., NATIONAL UNIVERSITY OF SINGAPORE;

M.Eng., MASSACHUSETTS INSTITUTE OF TECHNOLOGY)

A THESIS SUBMITTED

FOR THE DEGREE OF DOCTOR OF PHILSOPHY

NUS GRADUATE SCHOOL FOR INTEGRATIVE

SCIENCES AND ENGINEERING

NATIONAL UNIVERSITY OF SINGAPORE

2014

# Declaration

---

I hereby declare that the thesis is my original work and it has been written by me in its entirety. I have duly acknowledged all the sources of information which have been used in the thesis.

This thesis has also not been submitted for any degree in any university previously.

_____

Loh Iong Ying

15 August 2014

# Acknowledgements

First and foremost, I would like to express my heartfelt gratitude to my thesis advisor, Dr. Wang Zhisong, for his patient guidance and constant encouragement throughout my PhD study. Besides his immense knowledge and critical mindset that are always reliable, he has taught me many valuable life lessons and important research attitude that could not be learned in textbooks. To sum my graduate experience with one sentence, this thesis would not be possible without his support.

I would also like to extend my thanks to the thesis advisory committee members: Dr. Zhang Yong, Dr. Yan Jie and Dr. Liu Ruchuan, for their constructive feedbacks and comments. I wish to acknowledge National University of Singapore and Ministry of Education for funding this project. I am grateful to NUS Graduate School for Integrative Sciences and Engineering for providing me this great opportunity in the first place.

The assistance provided by post-doctorate fellow Dr. Sarangapani Sreelatha in completing the initial experiments of my project was greatly appreciated. I would also like to acknowledge Onittah Lola Nair for helping to obtain the data shown in Figure 37.

I would also like to thank Dr. Hou Ruizheng, Dr. Cheng Juan, and Liu Meihan for their insightful discussion and moral support. Their companionship made my rough PhD life much more enjoyable.

I am blessed with the love and support of my family, especially my parents Loh Mong Eng and Tham Gee Lan, and my partner, Yeo Hsiao Lun. Their kind understanding and patience had reminded me that I am not alone in this journey.

Finally, I would like to thank all that who had helped me to complete my experiments and thesis in a direct or indirect manner.

# Contents

# Summary

Motor proteins like kinesins, dyneins, and myosins are molecular machines that convert chemical energy to mechanical work, driving many important biological processes. They are bipedal nano-walkers that selectively dissociate the rear leg and bias it for a forward binding so as to make directional steps along a linear track. Inspired by these biological nanomotors, artificial track-walking nanomotors are actively developed and could be critical for the next industrial revolution, in parallel to steam engines for the previous industrial revolution two hundred years ago. Despite the efforts, the field of track-walking nanomotors remains small and difficult, a sharp contrast to the wide-spread success of simpler switch-like nanodevices. One of the reasons is that all track-walking nanomotors reported use a single molecular motif for the wheel-like binding component and also the engine-like component responsible for energy consumption and force generation. This contrasts with macroscopic motors such as modern cars, which are characterized by spatially and functionally separable engines and wheels. Such a modular design is desired to reduce the technical requirements and fill the nanodevices-nanomotors gap.

This project proposes a general design principle of modular nanomotors constructed from untangled engine-like and wheel-like motifs, and provides an experimental proof of concept by implementing light-responsive bipedal DNA nanomotors. The engine of the DNA nanomotors is azobenzene-tethered

hairpins, which absorb light of different colours to achieve a bi-state switching that mechanically dissociates the legs from the track for motility. The two legs of the nanomotors are identical, yet bind asymmetrically to a DNA duplex track with identical binding sites. This asymmetric binding is essential for selective rear leg dissociation. By tuning the design of binding sites, the nanomotors could be made to move under different conditions and up to different levels of performance. The forward bias for leg binding is also achieved. Besides, the nanomotors are waste-free and beyond the previously reported burn-the-bridge motors. The modular design principle is versatile, potentially opening a viable route to develop track-walking nanomotors from numerous molecular switches and binding motifs available from nanodevices research and from biology. Hence the field of track-walking nanomotors is expected to expand drastically.

# List of Tables

# List of Figures

---

xii

# Chapter 1   Introduction

## 1.1   Biological nanomotors

Motor proteins from the kinesins, dyneins, and myosins superfamilies drive many biological processes such as intracellular organelle transport, cell division, and muscle contraction (*1–5*). Kinesins and dyneins move along microtubules, while myosins move on actin filaments. They convert chemical energy, obtained from hydrolysis of ATP (adenosine triphosphate) bound to them, into mechanical work. Members from the three superfamilies do not necessarily share the same characteristics. For example, kinesin-1 and kinesin-14 from the kinesin superfamily walk in opposite direction, and myosin-V is a processive motors and myosin-II responsible for muscle contraction is not. For the scope of this project, the discussion of biological motors will be limited to processive nanomotors from each superfamilies: kinesin-1, myosin-V and cytoplasmic dynein. They are bipedal molecular walkers that selectively dissociate the rear leg and bias it for a forward binding, making directional steps along a linear track.

Kinesin-1 is a homodimer walker with two identical heavy chain heads (or feet) that bind to ATP and microtubules. The feet are connected to a neck-linker that is responsible for power stroke by conformation change. The neck-linker is then connected to a coiled coil and finally to the cargo-carrying domain. Kinesin moves in a hand-over-hand fashion with about 8 nm centre-

of-mass step size (*6*). Myosin-V is very similar to kinesin in structure and movement mechanism (*7*, *8*), but with a few key differences. Myosin is larger than kinesin and has a much longer rigid neck-linker domain that is sometimes referred as the lever arm (*8*, *9*). Myosin has a step size of 36 nm and walks hand-over-hand (*10*, *11*). For kinesin, the conformational change for power stroke occurs during ATP binding; for myosin, during inorganic phosphate (Pi) release. Both motors feature a singular component (motor domain) that highly tangles energy injection mechanism (ATP binding) and track-binding (microtubules or actin filaments). On the other hand, cytoplasmic dynein (Figure 1) from the dynein superfamiliy has an energy-consuming facility (motor domain) that is separated from the track binding components (microtubule-binding domain) (*12*).
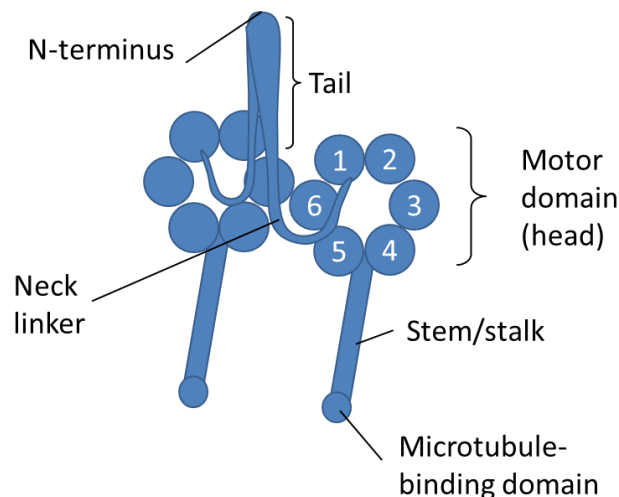


**Figure 1 Structure of a cytoplasmic dynein.** The motor domain has six AAA modules; AAA1-4 can bind to ATP but the exact mechanism is unknown. N-terminus is believed to provide the power stroke (*13*). Adapted from ref. (*14*).

The motor domain of dynein, made of six AAA modules (ATPases Associated with diverse cellular Activities), is like an engine consuming ATP

to perform mechanical work (*13*). AAA1 is generally accepted as the main site of ATP hydrolysis and have direct interaction with microtubules. ATP binding causes dynein to dissociate from the microtubule, with dynein assumes a pre-power-stroke conformation with the stalk tilted upwards and further towards the minus end (a step forward) (*15*). The later hydrolysis of ATP to ADP and Pi will cause the linker to reattach to the microtubule. This binding accelerates the release of Pi from AAA1, and causing the linker to return to its previous form (post-power-stroke). Finally, the cycle restarts after the ADP is released.

Dynein was found to take shorter steps under load (*12*): at zero load dynein predominantly takes 24 nm and 32 nm steps; at low load (< 0.4pN) dynein has a step size of 25 nm; and at high load (> 0.8pN) dynein takes even shorter steps of 8 nm. A recent finding of two dimensional step size further suggested that there are two modes of stepping for dynein (*16*). When the two motor domains are close together, the movement is uncoordinated. The stepping becomes coordinated when motor domains are separated by a larger distance. Qiu and coworkers proposed that the coordination arises from tension based mechanism (*16*).

Dynein does not necessarily walk in a hand-over-hand fashion, unlike myosin and kinesin, to achieve processivity (*13*, *16*).

## 1.2 Artificial DNA nanomotors

DNA (deoxyribonucleic acid) strands are made of nucleotides that each are composed of one sugar group, one phosphate group and one base. The deoxyribose sugars and the phosphates form the backbone of the DNA and the bases are responsible to form hydrogen bond with bases from another DNA strand. There are four bases, namely adenine, cytosine, guanine and thymine (A, C, G and T). Complementary bases (A-T and C-G) from two DNA strands could hybridize to form a duplex, with a shape of double helix (*17*). C-G base pair is stronger, as it is bound together by three hydrogen bonds, while A-T has two hydrogen bonds. The specificity of base-pairing leads to predictable DNA structure and becomes the basic of the formation of DNA nanomotors and tracks.
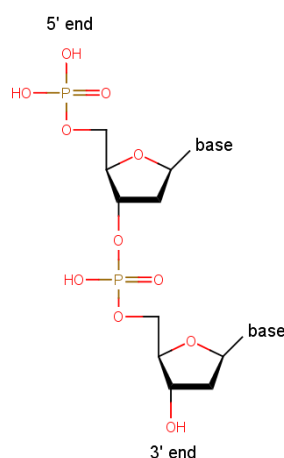


**Figure 2 Schematic drawing of a two-nucleotide single-strand DNA.** The bases are connected to the deoxyribose sugars that are linked together by phosphate groups. The sugar-phosphate backbone is negatively charged and has polarity of 5' end to 3' end. The 5' end and 3' end are labelled according to the naming of carbon in the sugar group. Two single strands in a double helical duplex are anti-parallel.

4

Inspired from the biological motor proteins, DNA nanomotors were first demonstrated as bipedal fuel-driven nanomotors that walk along DNA tracks in 2004 (*18*, *19*). Nanomotors operate in an environment that has a constant temperature. The second law of thermodynamics dictates that a net supply of energy must be provided to the nanomotor system for directional motion. Besides, the movement of a nanomotor is governed by the free energy changes under the isothermal condition. In equilibrium, the motor binds to the track and the motor-track system achieves a configuration with lowest free-energy state. The energy supply is then injected to push the motor-track system to a higher free-energy state that favours leg dissociation. After that, the motor spontaneously decays to a lower free-energy state resulting in a leg binding. The motor then must be able to recover the original lowest energy state to make a step, forming a movement cycle for continuous motion.

Before discussing and comparing artificial nanomotors (which will be limited to track-walking DNA nanomotors only, please see ref. (*20*) for synthetic molecular nanomotors), a few characteristics are important to be identified.

Processivity is the ability of a nanomotor to not completely detach from the track during its movement. This parameter becomes important for such a small scale, since gravity is a negligible factor and Brownian motions become dominant. Processivity is usually measured in number of steps or travel distance made. Wild-type kinesins show a typical travel distance of about 1 μm (hundreds of steps, corresponding to a probability of track-attachment of

about 99%) and velocity in the order of 0.1 to 1 $\mu m \cdot s^{-1}$ depending on ATP concentrations (*21–24*). Myosins and dyneins also share similar performance (*25*, *26*). Reported artificial motors typically exhibit processivity of a few steps (< 100 nm) and typical velocities in the order of 0.1 to 1 nm/min, which are few orders of magnitude slower.

Ratchet is a selective detachment mechanism, and in terms of nanomotors, it is the ability to detach the rear leg while the front leg remains bound to the track. The key to realize this mechanism is asymmetrical binding by either asymmetrical legs or symmetrical legs. Asymmetrical legs are relatively easy to achieve as it requires only unique sequences for each motor's leg and track's binding site combination, but it will limit the extension of the motor to travel for a larger distance, since each steps made will introduce one more combination. Therefore, symmetrical legs, found in biological motors, which induce different front and rear leg bindings are preferred. Nanomotors with ratchet could only achieve a maximum of half directionality, as the motor can either rebinds to the original state or move forward after the rear leg is dissociated. Power stroke is a necessary mechanism for a motor to have a higher forward steps to backward steps ratio. This forward bias could be achieved by introducing a different backward and forward distance for the motor or have a conformation change such that the nanomotor leans forward during detachment of rear legs.

Directionality measures the ability of a nanomotor to move preferentially towards one end of a track. Most of the reported artificial motors employed

shortcuts to achieve forward bias and eventually directionality: destroying one of the two possible paths, or in other words, adopting the "burn-the-bridge" approach. A new equilibrium is created after each step by eliminating the backward path (the track could have periodic binding sites), and forcing the motor to make a forward step. High directional fidelity (*27*, *28*) could be achieved if there is integration of rear leg dissociation (ratchet) (*29–37*), and forward bias (power stroke) (*22*, *31*, *37–40*).

The motility and directionality of nanomotors are mainly observed by visualisation of DNA structures in gel electrophoresis (*18*, *29*, *41–45*) (especially burn-the-bridge motors since each movement modified the whole DNA motor-track structure), fluorescence spectroscopy that observes either the signal from FRET pair or dye-quencher pair (*19*, *29–31*, *41*, *46*), and a rare method of surface plasmon resonance (*47*). These measurements are generally ensemble measurements, as the system contains many nanomotors and tracks. Recently, AFM was also employed to monitor the movement of a single nanomotor (*48–50*).

Autonomous operation is also a sought-after feature. It means the molecular motors could continually operate as long as the system is initially supplied with sufficient energy, without the manual application of external stimulants (*7*).

One important feature lacking in artificial nanomotors is the modular design found in cytoplasmic dynein. Reported artificial nanomotors have

inseparable energy consumption component responsible for force generation (the engine) and nanomotor's leg-track binding component (the wheels). In other words, energy required to selectively detach the rear legs is injected directly into the track-binding rear legs. Unlike kinesins and myosins that are refined by nature, the technical difficulties of a singular component that could perform both functions well at the same time are rather high. To draw an analogy to modern cars: modular design easily allows the car's engine to be exchanged for a higher horsepower one without the need to change the wheel.

## 1.3   Nanomotors with inseparable engine and wheel components

### 1.3.1  Fuel-driven nanomotors

The fuel-driven nanomotors feature bipedal nanomotors walking by binding to single-strand sites of the track. They employed unique fuel strands, which are only complementary to one specific combination of the track site and motor's leg, to join the motor's leg with the binding site. The motor's leg could be selectively detached from the track by applying a complementary second fuel strands to remove the first fuel strand. Thus, energy from DNA hybridization of the two fuel strands was injected at the binding legs site to dissociate the legs. Forward bias was acquired because the nanomotors were guided manually (adding suitable fuel strands) to follow the one directional track.

Sherman *et al.* produced an inchworm motor (Figure 3), because the motor's front leg always leads the rear leg (*18*). When the system was

irradiated with UV, the psoralen will covalently link the motor's leg and the track site. Shin *et al.* fabricated a hand-over-hand motor, as the rear and front leg exchange leading role (Figure 4) (*19*). Each binding site is labelled with a different fluorescent dye and the motor's leg with quencher. If the two meet, the dye signal will decrease.
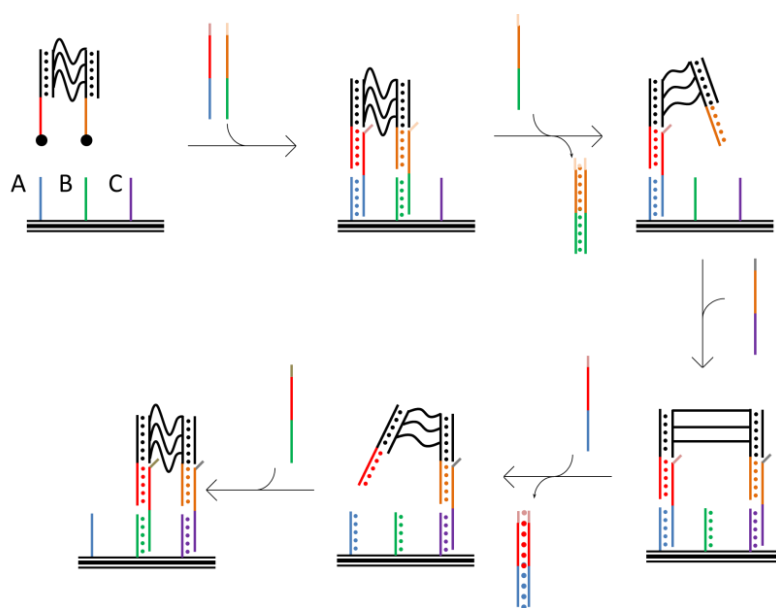


**Figure 3 Non-autonomous inchworm walker.** The system has three components: a rigid triple-crossover track with three sites; a bipedal walker with psoralen tags (black dot, removed later for clarity); and fuel strands with their complementaries. Two fuel strands with unique sequence binds specifically to A and B sites. The fuel complementary frees the front leg by initiating hybridization via sticky ends at the fuel strand. Another fuel strand is introduced that binds the front leg to C-site. Similarly, the rear leg moves to B-site and another duplex waste is produced. The matching colours indicate complementariness.

The key differences in these two reports are the movement mechanism and the methods characterizing on the movement of the DNA nanomotors. Sherman's version needed an extra step for detaching the front leg and allowed it to re-attach to a forward binding site; whereas in Shin's version, the rear leg detaches, diffusively searches and hybridizes to a forward binding site.

Sherman and co-workers used gel electrophoresis to characterize complex formed at different stages with the help of Psolaren tags, while Shin used real-time fluorescent spectroscopy to monitor the movement as the corresponding signal changes.
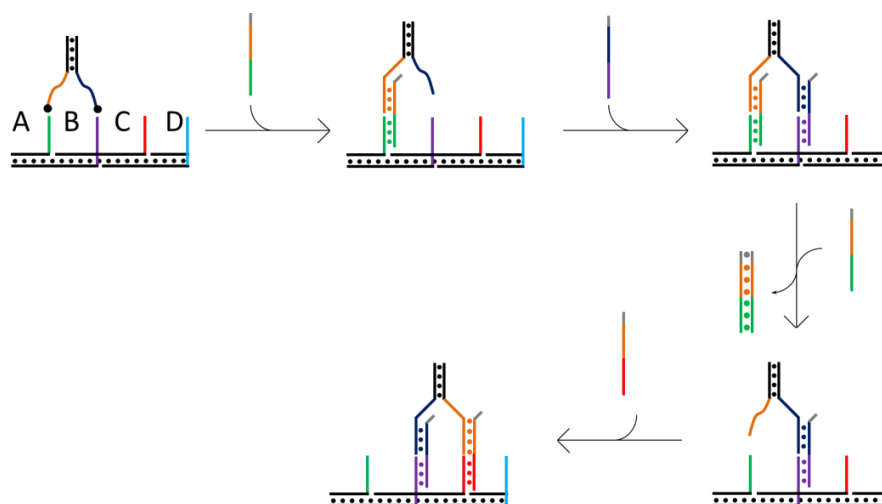


**Figure 4 Hand-over-hand DNA-walker.** The system has three components: a double-strand track with four sites, each labelled with a different fluorescent dye; a bipedal walker with quenchers (black dot); and fuel strands with their complementaries. The first fuel strand binds the walker's leg to the track specifically via A site, then the second fuel strand binds the other leg. The fuel complementary frees the rear leg by initiating hybridization via sticky ends at the fuel strand. Another fuel strand binds the rear leg to C-site. Similarly, the rear leg moves to B-site and a duplex waste is produced. The matching colours indicate complementariness.

Contrary to the asymmetrical legs shown above, the concept of asymmetrical bindings of symmetrical motor legs was demonstrated by Green *et al.* in 2008 (*29*). The nanomotor was a duplex with two identical long sticky ends (legs) that could bind to the single-strand track with repeated binding sites (Figure 5). Competitive bindings occurred between the front and rear leg because of the lack of full complementary bindings. Under the right condition (left foot lifted up to reveal a sticky end domain) was met, the hairpins will

selectively dissociate the rear legs. However, forward bias is not present here because the detached leg could be bound to either a forward or backward site. The next year, the same group replaces the second fuel with nicking enzyme N.BbvC IB that will cut and remove the first fuel strand from the motor (*41*).
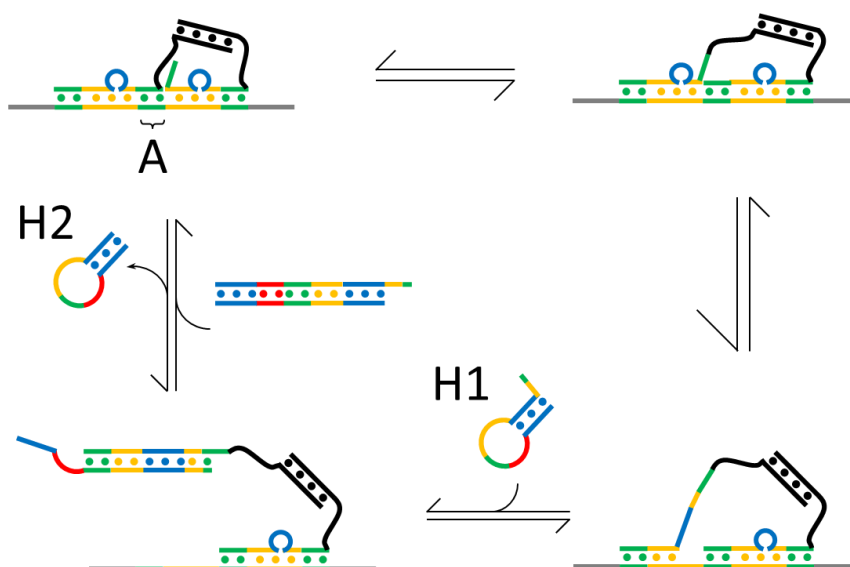


**Figure 5 Fuel-driven symmetrical nanomotor.** The system has three components: a single-strand track with repeating binding sites (green-yellow); a bipedal walker with symmetrical legs; and two hairpin fuel strands (H1 and H2) that complement to each other. The two legs will compete for the same binding domain (A) for a full leg binding. Half of the time, the left foot will be lifted up to reveal a sticky end domain. This will bind to the complementary sticky end of H1 and initiates a strand displacement reaction that opens the stem of H1, subsequently dissociates the left foot from the track. Part of the opened loop H1 acts as a second sticky end to initiate hybridization with H2 to form the H1H2 duplex waste. The free leg could then backward or forward in equal probability. The matching colours indicate complementariness.

In 2009 Omabegho *et al*. group introduced a relatively sophisticated fuel-driven nanomotors on a periodic track, albeit it was burn-the-bridge (*42*). Ratchet was attained due to asymmetrical legs; forward bias was attributed to the backward path blocked by the fuel strands. The track in this work is of

double-crossover structure that gives a better rigidity and could accommodate more binding sites or a larger motor.

### 1.3.2 Cleaving nanomotors

Cleaving nanomotors consume the periodic track while they walk on them; this process ensures a specific direction with a pre-defined landscape. However, without a fixed starting point, the molecular motor's direction is dependent on the starting position. For example, if the motor was first bound to the left end of the track, the motor will move to the right and vice versa. Perhaps the most prominent cleaving nanomotors are those using an enzyme that only cleaves a particular target. In 2005, Bath *et al.* (*46*) used nicking enzyme to cut a particular sequence from one strand of a DNA duplex and Tian *et al.* (*43*) used DNAzyme to cut RNA that has been inserted into the DNA strand (Figure 6). The movement is achieved by cleaving the current target site, exposing the motor leg and destabilize the existing motor-track binding. Then, the motor's leg will search and bind to the next full binding site that promotes a lower energy configuration. This process, strand replacement through branch migration, is repeated until the motor moves to the end of track. This class of DNA nanomotors is obviously burn-the-bridge and autonomous. The verification of motor movement is similar to previous experiments with Bath using a dye-quencher pair and Tian, gel electrophoresis.
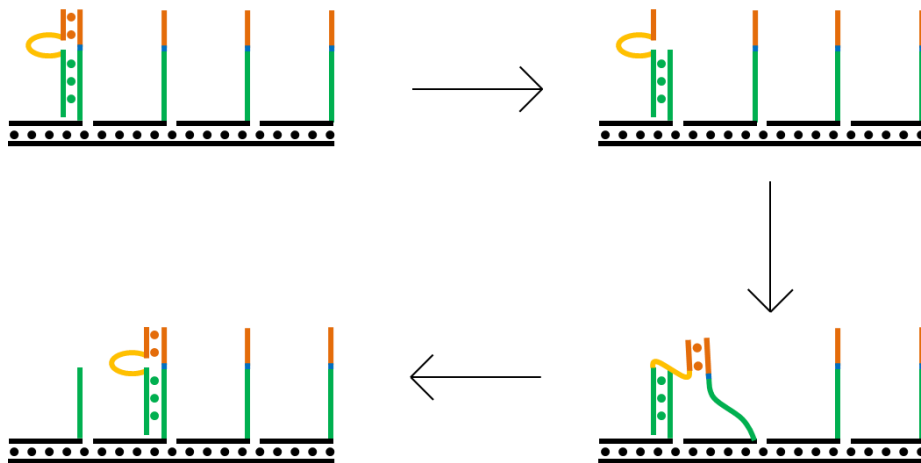
**Figure 6 DNAzyme nanomotor.** The track is mainly made of DNA with only the bonds to be cleaved replaced by RNA sequence (blue). The catalytic core (yellow) will cleave the RNA and branch migration happens. The matching colours indicate complementariness.

Further extension to the DNAzyme molecular nanomotors is a multiple-legs nanomotor first presented in 2006 (*47*). As the number of legs increased, the processivity is increased because the chance of dissociation of all legs together is lower. In 2010 (*48*), an improved version was made with an additional leg was allocated for anchoring at a designated starting point. DNA origami is used here to construct a large and complex track. Together with the pre-defined track, the directionality is assured with an increased processivity. Recent development substitutes the DNAzyme and RNA with Pyrene and a disulphide bond, respectively (*44*). By this replacement, the motor could be light-operated by pyrene-assisted photolysis of disulphide bonds, the motors then move forward by binding to a longer track site.

### 1.3.3  Light-driven nanomotors
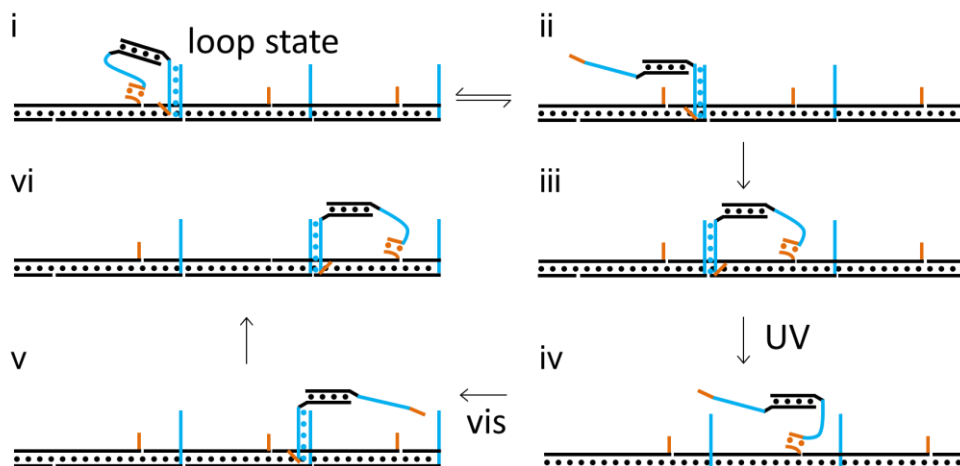


**Figure 7 Light-driven bipedal nanomotor.** The system has two components: a double-strand track with three composite sites and a quencher at the end, and a bipedal motor labelled with dyes at the end of the legs. The leg of the motor composed of two parts: a longer azobenzene-tethered leg part (blue) and a shorter strand (orange). The motor will form asymmetrical bindings as shown in state iii since it has a lower free energy. During UV irradiation, the rear leg will be detached (state iv). Then, with visible light irradiation, the front leg will bias forward via branch migration (state v), and the free leg will either bind to a forward site (state vi) or on the same composite site (the loop state, state I, lowest free energy state). The loop state could also occur initially but the orange leg part could be dissociated by thermal fluctuation and reached state ii for further motor movement. Loop state traps the nanomotor but will not compromise the directionality. The matching colours denote complementariness.

A nanomotor that utilized light-responsive azobenzenes (see section 1.5.2 for further details) was presented by Cheng *et al.* in 2012 (*30*). The nanomotor is similar to Green's fuel-driven version (*29*), as it was also made of a duplex with two identical legs. The track was in duplex structure and has two protruding sticking ends that serve as one composite binding site for the nanomotor (Figure 7). The length of the duplex body was designed such that the nanomotor spans across two composite binding sites with asymmetrical bindings. The nanomotor moves under alternating visible and UV light irradiation. The ratchet was provided by the asymmetrical bindings of the

nanomotors and the forward bias was achieved by the branch migration. It was later experimentally proven (*31*) that ratchet and power stroke are presented in the system and the length of the body duplex, which in turn influence the formation of the loop state and the cross-site asymmetrical bindings, affects the performance of the nanomotor.

### 1.3.4 Others

One motor-track system that does not really fit in any of the classifications above comes from Yin *et al.* in 2004 (*45*), which uses repeated ligation and cutting of the nanomotor. The movement along the track involves the destruction or reconstruction of the "motor". Ligation was first used to join the two binding sites together with the motor. Then, a restriction enzyme (PflM I) was used to cut a specific sequence of the motor, restoring the initial motor structure but the motor was moved to second binding site. The third step repeats the ligation, but used a different enzyme (BstAP I) for cutting because of the different recognition site needed to maintain the motor structure. This is similar to the fuel-driven nanomotors involving unique strands in section 1.3.1, as many more different enzymes are probably required for each additional step for different recognition cutting sites.

## 1.4 Asymmetrical bindings usable for wheel-like components

Asymmetrical binding, either by identical or different legs, is a crucial condition for selective dissociation, and thus directionality, of track-walking

nanomotors. The requirement is higher for nanomotors with identical legs that move along a track with periodic binding sites. At least two different conformations or structures for the leg-site binding have to coexist and react differently to the same energy injection mechanism. For example, ATP will specifically bind to the rear leg of kinesin, causing it to detach more easily, even though kinesin has identical legs.

Besides introducing competitive binding domain for two identical legs as discussed earlier (Figure 5), another way to form asymmetrical bindings with identical legs is utilizing the polarity of single strand DNA. By pulling the different ends of the two strands in a duplex, the DNA can either unbind in an unzipping or shearing geometry (Figure 8). The force required to break the duplex with shearing geometry is three times larger than the same duplex with unzipping geometry (*51*).

Another literature suggested that the force required to break a duplex with shearing geometry depends on the length of the duplex and it is estimated to be about 20 pN by extrapolating the data in ref. (*52*) to 10-bp duplex relevant to the present motor. Unzipping breaks the duplex base pair by base pair (*51*) and the magnitude of unzipping force depends on the type of base pairing (*53*) (9 pN  for A-T is and 20 pN for C-G, giving an average of about 14.5 pN). By the above estimation, the force pulling the front leg is probably 1.4 times higher than the force pulling the rear leg for the present motor.
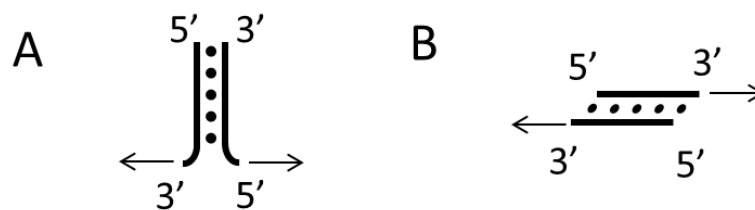
**Figure 8 Two duplexes with the same sequences but different geometries.**
A. The 5' end and 3' end from two DNA strands in a duplex were pulled apart will cause unzipping to occur as the base pair is opened up one by one. B. If the same ends (either the 5' or 3' ends) were pulled, it is a shearing geometry. The forces required to break these two geometries are very different.

Other possible candidates for asymmetric binding are proteins that will bind differently to DNA (*54*).

## 1.5   Nanodevices potentially usable as engines for motors

The nanomotors presented above used a singular motif for engine-like and wheel-like functions, and combining both functions into a singular molecular part limits the development of track-walking nanomotors. In comparison, there are many more bi-state switches, including synthetic molecular shuttles that switch between two binding sites (*55–59*), chemical structures that will vary between two lengths (extension and contraction) (*60–63*), structures that switch between two conformations (*64, 65*), and so on. Modular design found in dynein and modern cars will be beneficial to fill the gap between the nanomotors and switching nanodevices since many of these devices are already qualified as nanoscale engines. Synthetic molecular devices are beyond the scope of this thesis and will not be covered. A few research works

on DNA nanodevices, which particularly involved extension and contraction, were highlighted below.

## 1.5.1  Fuel-driven tweezers

A fuel-driven switch was demonstrated by Yurke *et al.* (*66*) using strand displacement via sticky ends (Figure 9). This DNA tweezer could be repeatedly opened and closed as long as DNA fuel F and its complement F* are provided. The extension is as long as the foldable duplex (black part in Figure 9) minus the width of the double duplexes and it was estimated to be about 6 nm. Lubrich *et al.* incorporated multiple DNA tweezers of the same kind into a long track that contracts and extends as DNA fuels and their complementaries were added (*67*). Since one DNA tweezer used contributes a 10 nm extension, and the total extension is amplified by the number of tweezers integrated.

Fuel-driven switches are not limited to translational extension-contraction as Yan *et al.* demonstrated a rotational switch using the interconversion between two topological double helices: paranemic crossover PX DNA and its topoisomer $JX_2$ DNA (*68*). By adding a set of fuel strands, PX motif could be converted to $JX_2$ motif that has its bottom rotated 180° relative to the PX motif.
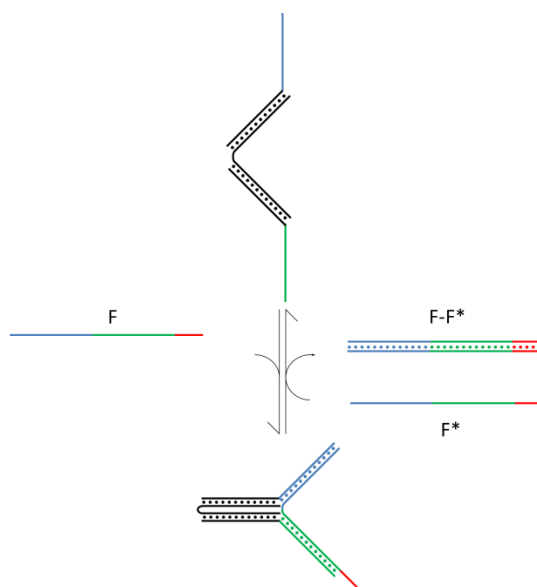
**Figure 9 DNA tweezer.** DNA strand F hybridizes with the dangling ends (blue and green) to pull the tweezers closed. Its complementary F* hybridizes with the sticky ends of F (red) to allow a formation of a relatively inert double-strand duplex F-F*. This revert the tweezer to an opened position as before. The reaction will continue until either F or F* is depleted.

## 1.5.2 Light-driven hairpins

The first photoregulation of the duplex formation of oligonucleotides was reported in 1999 (*69*). It was done by incorporating azobenzene via D-threoninol linker into one of the strands of the DNA duplex (Figure 10). Azobenzene switches from planar *trans* to non-planar *cis* conformation upon UV irradiation (absorption maxima at 320 nm (*70*) or 350 nm (*71*)). This transition will disrupt the stability of the DNA duplex. The *cis* form could isomerize back to *trans* form spontaneously in dark (thermal fluctuation) or by visible irradiation, but photoisomerization occurs much faster than thermal fluctuation (*70*). The maximum amount of the *cis* form induced by light irradiation is around 70 to 80% (*71*). Azobenzene is also photostable as the decomposition is negligible after prolonged irradiation.

19
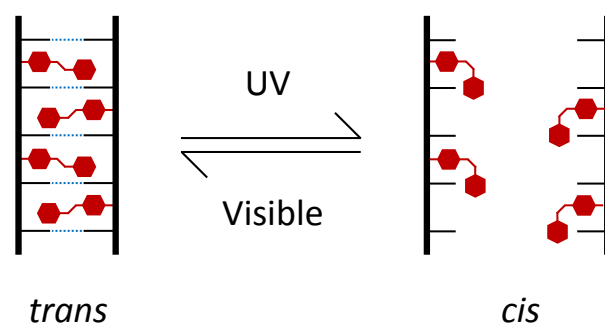
**Figure 10 Schematic illustration of photoregulation of DNA duplex formation by azobenzene.** The red hexagon pairs depict the azobenzenes tethered to the backbone of DNA strand and their conformation. The black lines are the base pair formed by hydrogen bond (blue dashed lines). UV irradiation (320 to 380 nm (*72*)) will change the conformation of azobenzene and disrupt the formation of hydrogen bonds, and breaking the duplex into single strands. Conversely, visible light irradiation (> 400 nm) promotes the reformation of the duplex.

In 2009 Asanuma's group improved the photoregulation by incorporating azobenzenes into both of the strands of the DNA duplex (*72*). In this paper and the one reported by Kang *et al.* (*73*), the incorporation of azobenzenes into hairpin was also demonstrated, UV irradiation will change the conformation of the azobenzenes in the hairpin stem, thereby opens up the hairpin and extends it into a single DNA strand. It was shown in Kang's work that increasing the azobenzenes in the stem improves the photoregulation, but the limit is that azobenzene moieties should be separated by at least two nucleotides (*74*). Since the hairpin width is about 2 nm and the number of azobenzene moieties inserted to the stem could be increased as the stem gets longer, the extension achievable by this nano-switch can be as long as the opened hairpin.

### 1.5.3 G-quadruplex and i-motifs

Found in vertebrate telomere, guanines in repeated sequence TTAGGG is known to form G-quadruplex structure by Watson-Crick and Hoogsteen hydrogen bonding, and bound together by a central monovalent cation (Figure 11) (*75*, *76*). The stability of the quadruplex formed is dependent on the species of the central cation and addition of other multivalent ions such as $Mg^{2+}$ (*75*). Alberti (*77*) has utilized complementary DNA fuels to switch between the compact G-quadruplex and duplex, which will extend from about 1.5 nm to 7.1 nm within seconds. Similar technique has also been applied on aptamer sequence as well (*78*). Later, Mayer *et al.* modified one guanine to be caged by a photo-labile protecting group, which will block the formation of quadruplex without light irradiation (366 nm) (*76*).
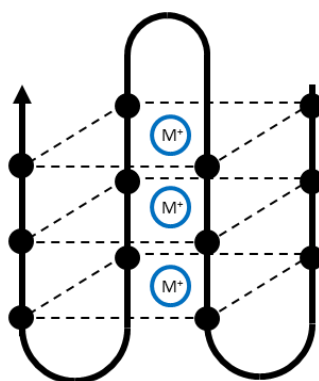


**Figure 11 Schematic drawing of G-quadruplex structures.** The $M^+$ represent the central monovalent cation, normally potassium ion, required to form the G-quadruplex. The black dots are guanines; the arrows indicate the 3' end of the DNA strand.

The complementary of G-quadruplex, or i-motif, could also form quadruplex under slightly acidic condition (pH 5) and opens up at pH value of more than 6.5 (*79–81*). The difference from G-quadruplex is that the structure

is held together by proton instead of cation (*82*). If complementary duplexes are supplied, the extension is about 5 nm, with estimated forces of 10 to 16 pN. Both G-quadruplex and i-motif can be characterized using circular dichroism spectrum (*83*, *84*). The opening and closing of i-motifs require a periodic change of pH value, which could be automatically achievable by using a chemical oscillator, Landolt reaction (*85*). However, the period for this pH variation is about 1 hour, which limits the nanomotors' speed.

## 1.5.4  Inductive coupling nanocrystals

DNA melting is a routine process to separate DNA duplexes, and thereby it would be valuable to have a localised temperature switch for DNA structures. Hamad-Schifferli *et al.* applied radio-frequency magnetic field to inductively heat a gold nanoparticle that is covalently linked to a 38 nt (nucleotides) hairpin (Figure 12). Since the temperature of the gold nanoparticle is higher than the melting temperature of the hairpin, opening of the hairpin could be observed to be achieved within seconds. Since the heating is only limited to site that has gold nanoparticle, selective heating and dehybridization is attainable. However, the temperature generated by the radio frequency coupling is only about 35°C, which could limit the number of base pairs that could be broken.
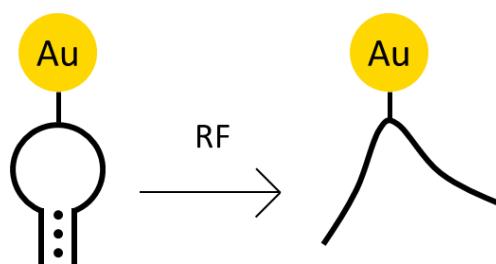
**Figure 12 Inductive coupling of a radio-frequency magnetic field to a metal nanocrystal covalently linked to DNA.** Radio frequency of 1 GHz is applied to inductively heat the 1.4 nm gold nanoparticles, which in turn dehybridize a 7 bp (base pairs) stem hairpin. The hairpin will reform after the magnetic field is removed.

## 1.6 Application of nanomotors

The challenge of nanotechnology at the present stage is to move from simple, switch-like nanodevices to track-walking nanomotors that perform a particular function, and finally to integrated nanomachines (*86–88*) of extended functionalities for real-world applications.

Gu *et al.* (*86*) demonstrated a nanoscale assembly line by integrating a similar fuel-driven nanomotor (*19*), a fuel-driven rotational switch (*68*), and a rigid DNA origami 2D track (*89*). The nanomotor presented receives three different cargoes from three cargo-holding stations as it move towards one of the track. The rotational PX and JX$_2$ motifs were used to hold the cargo (gold nanoparticles linked to a single strand DNA), while the triangular walker has three hands to accept three different cargoes. When the walkers moves by adding corresponding fuel strands, the stations were made to rotate as well such that the gold nanoparticles are in close proximity to the walker. Thus, the walker could exchange the cargo by complementarily binds the nanoparticle-

linked strand. All the cargo holders and binding sites for the walkers are on the DNA origami.

Another application is synthesis in a sequence-specific manner. He *et al.* (*87*) fabricated a ribosome mimetic using DNAzyme-based nanomotors (*43*). The binding sites of the track are attached with amino acid NHS esters. By attaching amine group on the DNAzyme walker, the walker could trigger amine acylation that transfer the amide group to the walker. Multiple steps would result a synthesis of oligoamides in a sequence desired. In a similar fashion, synthetic molecular shuttle was used to synthesise peptide (*88*).

## 1.7 Framework of thesis

### 1.7.1 Aim of study

The highly tangled wheel-engine is a feature largely borrowed from biological nanowalkers like kinesin and myosin superfamilies. Another family of biological nanowalkers called dynein keep the engine-like component distantly away from the track-binding wheel-like component, and the same engine component drives many nanomachines of diverse functions in living cells, suggesting possibility of modular designs for nanomotors like that of macroscopic cars.

The lack of a modular design for separable and modularized engine- and wheel-like components is a common impeding bottleneck at this early stage of nanomotor development. Two major technical requirements in artificial

nanomotors are an asymmetric binding mechanism for motion control and a bi-state contraction-extension switch for energy consumption and force generation. The two components need not be done by a single molecular part as reported for the previous artificial nanomotors; they instead may be separately implemented and optimized parts that could be flexibly assembled into nanomotors of many versions, just like the common practice in modern automobile industry.

This study intends to provide a viable route for the currently small and difficult field of track-walking nanomotors to access a larger molecular switches and binding motifs from the research communities of nanodevices and molecular biology as discussed earlier. This will potentially expand the field drastically in molecular systems, driving methods, mechanistic sophistication and beyond the burn-the-bridge designs.

Therefore, we propose and aim to apply a versatile modular design principle to track-walking nanomotors, which would be formed from functionally and spatially separable wheel-like components and bi-state switches as the engine. To achieve such goals, we chose to implement a light-powered symmetric DNA bipedal nanomotor.

### 1.7.2 Overview of thesis

Chapter 1 taps into the world of track-walking nanomotors by first examining the biological motor proteins, and followed by identifying the key

parameters required in discussing the performance of artificial nanomotors. These parameters are briefly compared to the biological counterparts. Then, a review of reported artificial nanomotors is presented by categorizing them according to the mechanism that drives the movement. Asymmetrical bindings and bi-state nano-switches are introduced because they could be integrated in a modular nanomotor design. Finally, the applications of nanomotors to create integrated nano-machines are discussed as well.

Chapter 2 lays forward the central principle for a versatile modular design. Developing around this idea, the various components to make a successful modular nanomotor are introduced, including the light-responsive azobenzene-tethered hairpins and the DNA sequence design and selection required. The methods to fabricate and verify the nanomotors and tracks are detailed, covering the native gel electrophoresis, absorbance measurements, and the motility measurements by fluorescence spectroscopy.

Chapter 3 and 4 demonstrate the two versions of the nanomotors and tracks. In the context, the detailed motor and track designs are discussed, together with the materials and methods used. The movement mechanisms for these two nanomotors are studied. The first motor version operates at low temperature, while the second motor has its legs modified to be operational at room temperature. The second version also introduces three dyes so that information of ratchet and power stroke mechanisms can be extracted.

Chapter 5 concludes about the nanomotors fabricated and compares the results to the initial aim. Possibilities for improvement are explored in the outlook of the current study.

# Chapter 2  Design and methods

## 2.1  Introduction
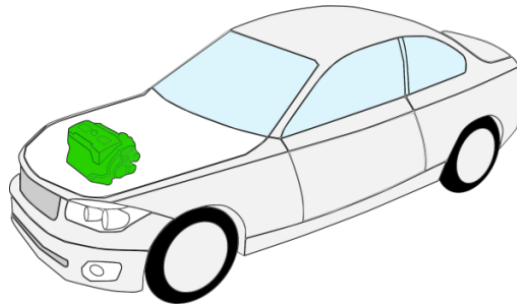


**Figure 13 Design principle of a modern car.** Modern cars employ modular design, having separable engine that provides the driving force and wheels that bound the car to the track while maintaining mobility. Artificial track-walking nanomotors reported to date have indivisible engine-like and wheel-like components, and this heighten the technical difficulty of improving the motor.

As mentioned in Chapter 1, virtually all artificial track-walking nanomotors reported to date use their track-binding components not only for directional rectification and gait control, but also for energy consumption and force generation. Nearly all the technical requirements are concentrating on this wheel-like component, which led to nanomotors extremely hard to make at this stage. Relatively, switching nanodevices are more common as compared to about a dozen of track-walking nanomotors reported, and development is largely stagnated at burn-the-bridge motors. Until now, there is no obvious way to directly integrate the engine-like switching nanodevices with a wheel-like track-binding component. This is a sharp contrast to macroscopic motors such as modern cars with separable wheels and engines. Perhaps the analogy is not straightforward because the wheels are always

attached to the road/track due to gravity; however, in nanoscale, gravity force is negligible and the motors require other forces to bind to the track.

## 2.2   A versatile design principle

The design principle, schematically illustrated in Figure 14 and Figure 15, applies generally to nanomotors with two identical legs and tracks with periodic binding sites. A major requirement is an asymmetric leg-site binding: a track-bound leg is dissociated more easily (*i.e.*, with a higher rate) by a force pulling the leg towards one end of the track than towards the opposite end. Then a symmetric motor can exploit the track's asymmetry in three distinctly different modes depending on the motor's size (Figure 14 I–III).
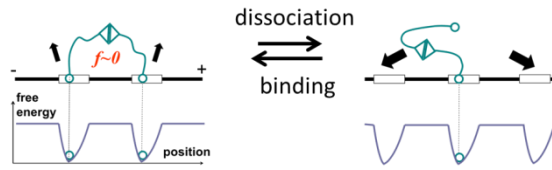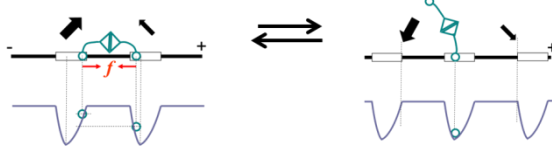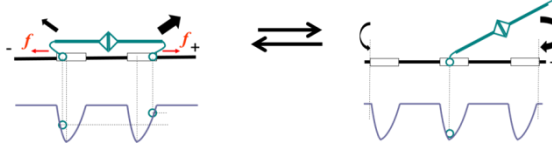
**Figure 14 Design principle of modular motor.**Three size-controlled modes of a symmetric bipedal nanomotor interacting with a periodic track of asymmetric binding sites. The motor and track are schematically illustrated in cyan and black; the underlying purple lines show the binding free energy between a motor leg (empty circle) and the binding sites (empty rectangles). A leg-site binding is asymmetric because it is broken more easily when the leg is pulled by a force towards one end of the track than the other end. This asymmetry amounts to a binding free energy that changes more steeply along one edge than the other. As an example, the two edges are shown here as harmonic oscillator potentials with a lower elastic constant for the edge near the track's plus end as indicated. The size of a motor limits its leg-track interaction to different modes: a short motor (compared to the binding site period) explores the two inner edges of adjacent sites (contracted mode); a long motor explores the two outer edges (expulsive mode). The same internal tension (f) of a two-leg bound motor causes more displacement along the less steep edge and does more work to raise the free energy, resulting in a lower barrier and hence a higher rate for leg dissociation along this edge than the other one (higher rates indicated by larger size for filled arrows). However, the dissociated leg accesses the less steep edge more easily, and binds the track along this edge at a higher rate. The dissociation and binding have opposite preference within either mode, yielding no net direction (detailed balance).
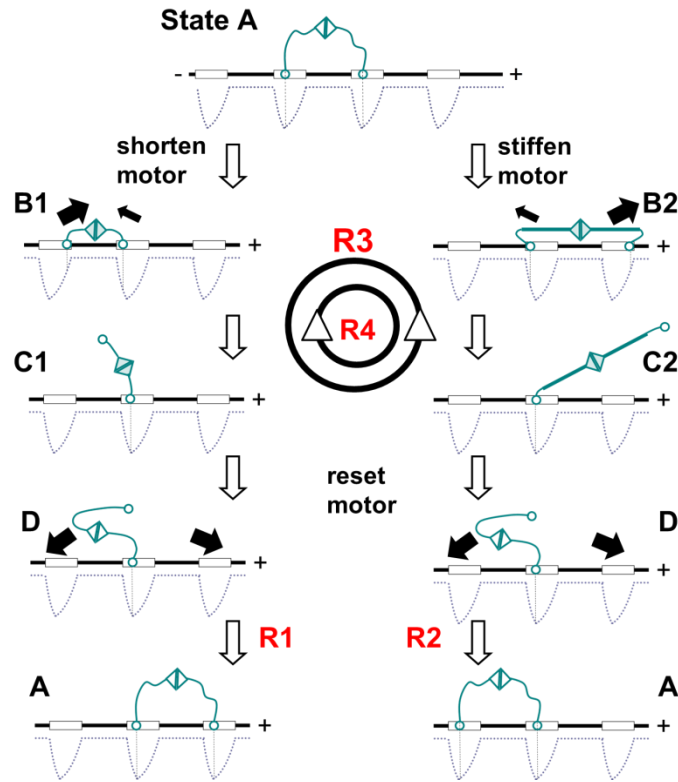
**Figure 15 Multiple regimes for a unidirectional motor by switching it between the modes.** The empty arrows indicate the operation cycles: A→B→C→D→A for regimes R1 and R2, A→B1→C1→C2→B2→B1→A for R3, and the reverse cycle for R4.

When the motor's size (*i.e.*, its average leg-to-leg distance) matches the track's binding site period, a relaxed mode occurs in which the two-leg bound motor has a low internal tension. Then the motor's two legs have equal chance for dissociation by thermal fluctuation regardless of the track's asymmetry. When the motor's size is smaller than the binding site period, a contracted mode occurs in which the two-leg bound motor develops an inward tension to pull the leg near the plus end (refer as front leg henceforth) backward but pull the other leg (rear leg) forward. The opposite pulling dissociates the rear leg preferentially, that is a higher dissociation rate for the rear leg than the front leg.

31

When the motor is longer than the binding site period and is rigid, an expulsive mode occurs instead: the motor's internal tension becomes outward to dissociate the front leg preferentially. Within each of the three modes alone, the motor has zero net direction as the detailed balance dictates that any site-selective preference for dissociation is balanced by an opposite preference for subsequent spontaneous binding of the dissociated leg. Hence the leg binding is preferred forward, backward and equal for both directions for the expulsive, contracted and relaxed modes, respectively. The details of dissociation and binding preference from a leg-site binding are explained in Figure 14.

Multiple regimes exist for making unidirectional motors by switching between the three modes to break the detailed balance. Four regimes are schematically illustrated in Figure 15 (marked from R1 to R4). For regime R1, alternately switching between the relaxed and contracted modes, e.g., by changing the motor's size between two values, makes a repeatable cycle in which the preference for rear leg dissociation in the contracted mode cannot be entirely compromised by the equal binding in the relaxed mode. This breaks the detailed balance to make a motor with a net direction towards the plus end. A motor with an opposite net direction is likewise made by switching between the relaxed and expulsive modes, e.g., by changing the motor's rigidity. This is regime R2. The R1, R2 regimes have a directional preference for leg dissociation but not for leg binding. Alternately switching between the contracted and expulsive modes leads to two new regimes with double preference for both dissociation and binding. If the motor's two-leg bound state in the expulsive mode (B2 in Figure 15) is more stable than that in the

32

contracted mode (B1), it is more likely that the switch from the expulsive to contracted mode induces leg dissociation and the reverse switch induces leg binding. Alternating both switches then automatically selects regime R3 in which the operation cycle is a preferred rear leg dissociation followed by a preferred forward leg binding. If instead the two-leg state in the contracted mode is more stable, the same alternating switches select regime R4, resulting in a reversed operation cycle and an opposite direction of the motor. We note that regime R1 was previously discussed in a theoretical paper [39].

## 2.3   Azobenzene-tethered hairpins

Azobenzenes, which were tethered to the DNA via D-threoninol linker (*74*), were used to drive the bi-state switch. One hairpin of the motor has a total of twelve light-sensitive azobenzenes (the design is modified from ref. (*72*), successful duplex opening by azobenzenes at room temperature has been demonstrated previously (*30*, *31*)). This light responsiveness allows us to elongate or shorten the overall motor length by opening (unwinding) or closing (winding) the hairpins, respectively. UV-light absorption by azobenzene creates a high-energy cis form that disrupts the formation of hairpins, unwinding the hairpins and increasing the overall length; visible light absorption switches it back to the ground-state trans form, which helps the rewinding of hairpin, generating a force in the process. The implementation of double winding hairpins is to ensure that the force is sufficient to break the binding between the motor leg and composite site of the track.
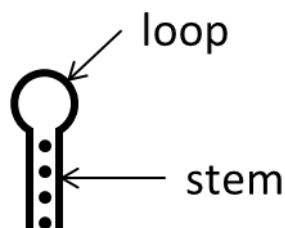
**Figure 16 Schematic structure of a hairpin.** The loop is single strand DNA, while the stem is formed because the strand is partially self-complementary. Azobenzene is incorporated into the side chain tethered to the nucleotides at the stem.

## 2.4  DNA sequence design

During sequence design and selection, normally a two-part strategy was deployed. Firstly, sequences for the motor and track strands were found using Computer-Aided Nucleic Acid Design pAckage (CANADA) (*90*). CANADA utilizes a fully automatic and graph-based algorithm to generate sequences from a pool of unique subsequences. A sequence pool is $n_b$-unique if each subsequence (maximum length $n_b$) of sequence with length $n_s$, and its complementary, occurs only once in the pool. The algorithm for generating the sequence required is to follow the path that links the subsequences and their successive ($n_b$-1 overlapping) subsequences. For example, a 15-mer that are 5-unique has common subsequences with length of at most 4-mer. One 5-mer is randomly selected from the pool as the starting node and the 5-mer with first four nucleotides overlapping with the former is one of the successive subsequences. The step is repeated until a 15-mer is generated. Therefore, $n_b$ uniqueness should be as small as possible to promote hybridization specificity for getting the intended structure of the motor and track. However, there is a minimum value of $n_b$ for a successful sequence generation, since longer

34

sequences require more subsequences in the pool. The result could be filtered based on the user constraints (GC ratio, forbidden sequences; *e.g.* GGG).

Next, Mfold web server (*91*) was used to predict possible secondary structures and their associated minimum free energies. DNA single strand is represented as semicircle with nucleotides as the vertices (*92*). The backbone between consecutive nucleotides is portrayed as the arcs of the semicircles and is named exterior edge. Base pairing (A-T or G-C) is depicted as a line connecting two vertices and is called interior edge. The interior edges are not allowed to touch or intersect with each other, which do not account for any possible pseudoknot formation. The faces, or the planar regions bound by the edges, are associated with a free energy. Depending on the type of edges that bound the faces, substructures such as hairpin loop, stacking legion, bulge loop, interior loop and bifurcation loop are defined (see ref. (*92*) for the exact definition). Invalid substructures would have their free energies set to infinitely high free energies; for example, hairpin loop with three nucleotides is sterically impossible. The total free energy of a DNA structure is the summation of free energies of its faces. The minimum free energies are computed recursively, which starts from five-nucleotide subsequences. The folded structural output is then examined to discard strand candidates that have unwanted secondary structures. As a general rule of thumb, if the structure has unwanted base pairing of more than five nucleotide pairs, the sequence generation by CANADA would be repeated.

Generally, Mfold is limited to the thermodynamics of a single strand DNA, but the motor and track are usually constructed from multiple strands. Therefore, NUPACK (*93*) was employed to predict the unpseudoknotted secondary structure for systems involving multiple strands. Extending from methods used in Mfold, multiple DNA strands could be arranged in a circle with no crossing lines (*94*). Therefore, calculation of the partition function and minimum free energy for different multi-strand secondary structures could be computed with consideration of distinguishability issues. The equilibrium concentrations for multi-strand complexes in a buffer could also be computed. This information is helpful in confirming the final structure of motor and track desired are the prominent species after annealing.

## 2.5   Motor-track fabrication

Component strand for motor and track were ordered from Nihon Techno Service Co., Ltd. and Integrated DNA Technologies, Inc., respectively. The samples were received in lyophilized form. The dry oligonucleotides were resuspended in TE buffer (10 mM Tris; 0.1 mM EDTA; pH 8.0) to a stock concentration of 100 μM. The stock solution was then stored at −20°C for further use. Component strands were annealed in appropriate buffers to produce the motors and tracks required. (Please refer to individual chapters for Motor Version I and II for detailed annealing procedures).

Tris solutions are weak basic buffers which keep DNA deprotonated and soluble in water. EDTA is a chelator of metal ions that is necessary for nucleases, and protects nucleic acids from degradation.

## 2.6 Gel electrophoresis

Gel electrophoresis is a well-known method to separate and purify biomolecules (*e.g.* DNA) in complex mixtures according to their sizes and charges. For this project, native polyacrylamide gel electrophoresis (PAGE) was employed to estimate the formation of the motor and track structure, since native PAGE preserve the DNA structure formed and polyacrylamide gels have a higher resolution than agarose gels. The nanomotors and tracks fabricated have single-strand sticky ends, and will have different mobility in acrylamide gels depending on the sequences and conformations (*95–97*). Therefore, the tracks and motors were compared to their incomplete, reduced by a step, counterparts and verified to have one prominent band.

Polyacrylamide gels are formed by the co-polymerisation of acrylamide monomers with smaller amount of cross-linking monomers, usually methylenebisacrylamide (bis). The polymerisation is initiated by free radicals provided by ammonium persulfate (APS) and TEMED catalyse the formation of radicals. The copolymerisation of these two components together produces a three-dimensional mesh. Polyacrylamide gels are characterized by the weight percentage of total monomers (acrylamide plus bis) T and cross-linkers percentage C. For example, a 30% 29:1 acrylamide/bis gel would have T of 30%

and C of 3.3%. If T increases and C remains constant, the pore size decreases (*98*). When T remains constant and C increases, the pore size follows a parabolic function with a minimum at C = 5%. Generally, C of less than 5% is used and C of 3.3% is common in dealing with native DNA structure.

A Mini-PROTEAN Tetra cell setup was used to cast the gel. Spacer plate of gel thickness of 1.5 mm and short plate were washed thoroughly with ultrapure water and then with ethanol before the plates were wipe-dried. The short plate was placed on top of the spacer plate to form a glass cassette. With the casting frame placed upright, the plates were slid into it. The short plate and spacer plate were aligned properly on a flat surface. The pressure cams were then snapped in place to secure the glass cassette. The casting frame with the secured glass cassette was then locked into position at the casting stand to be ready for gel casting. The glass cassette was checked to be pressed against the grey gasket to avoid any leaking.

| T (Gel %) | 29:1 30% acrylamide (ml) | $H_2O$ (ml) | 10× TBE (ml) | 10% APS (µl) | TEMED (µl) |
|---|---|---|---|---|---|
| 6 | 2.4 | 8.2 | 1.2 | 200 | 10 |
| 10 | 4 | 6.6 | 1.2 | 200 | 10 |

**Table 1 Composition of acrylamide gels with different gel percentage.** The listed gel percentages are the two gels used in the operation experiments. T was adjusted from the stock concentration of 30% to a suitable value to observe the DNA structure in the size range desired.

The monomers solution was prepared by combining all the reagents as shown in Table 1, except APS and TEMED. After APS and TEMED were

added, the solution was vortex-mixed thoroughly and quickly pipetted into the glass plates until the solution reached about 0.5 cm below the top edge of the short plate. A 10-well comb was inserted between the plates carefully to avoid any formation of bubbles. The acrylamide/bis solution was left for at least 30 minutes to solidify at room temperature.

After polymerisation was completed, the glass plates were removed from the casting stand and frame, and the comb was removed from the glass plates carefully as well. The gel cassette (glass cassette with formed gel) was placed with an angle onto the gel support of the electrode assembly, with the short plates facing inwards. When only one gel was used, a buffer dam, instead of another gel cassette was placed on the other side. The assembly was then put into the tank in a correct orientation according to the electrode terminals. The running buffer (1×TBE) was used to rinse the well and continuously filled until the liquid level reached the 2-gel line marking.

The Gel Loading Dye, Orange (6X) by New England Biolabs was loaded together with the DNA samples in 1:5 ratio, with a total of 3 μL. The loading dye contains colour markers and Ficoll-400. Colour markers allow visual tracking of DNA migration and Ficoll-400 increases the density of a sample such that the sample will settle to the bottom of the gel's well. Traditional glycerol was avoided because it can form complex with borate in TBE and distorts the DNA migration. Low molecular weight DNA ladder by New England BioLabs and GeneRuler 100 bp DNA Ladder by Thermo Fisher Scientific Inc. were used according to the size range desired.

The lid was then closed tightly. The electrical leads were connected to the power supply. The voltage was set to a constant value and the run time was adjusted accordingly. After the electrophoresis was completed, the power supply was turned off and the electrical leads disconnected. The tank lid was removed and the electrode assemblies were lifted out carefully. The running buffer in the electrode assemblies was poured off to the tank and stored for further usage. The gel cassette was removed from the electrode assembly carefully. The short plate was separated gently and then the gel was removed carefully to be stained. 50 mL of gel red (3×) was poured into a plastic box with the gel and was left on the rocker for 20 minutes. The gel was then taken out to be imaged in the Bio-Rad Gel Doc EZ system.

## 2.7   Absorbance measurement

The Beer-Lambert law states that the absorbance A of intensity of the light transmitted through an absorbing solution is related to concentration and the path length of the absorbing solution (*99*):

$$A = log_{10}\frac{I_0}{I} = abc \qquad (1)$$

where $I_0$ is the incident light intensity, I is the transmitted intensity, a is the molar absorptivity or the molar extinction coefficient, b is the path length, and c is the concentration of the absorbing species. Since b is usually 1 cm for a standard cuvette in spectroscopy measurement and a is constant for a certain species, the absorbance is linearly proportional to the concentration. This

relation is only true for dilute solutions (< 10 mM) (*100*), and the absorbance could be used to estimate the concentration of the absorbing entity present.

## 2.8  Motility measurement

Fluorescence describes the light emitting properties of a molecule that absorbs light of higher energy and emits light of lower energy. In this case, the molecule is a fluorophore, also known as a dye. A fluorophore with a higher quantum yield (ratio of fluorescence photons emitted to photons absorbed) is preferred as higher fluorescence intensity can be obtained.
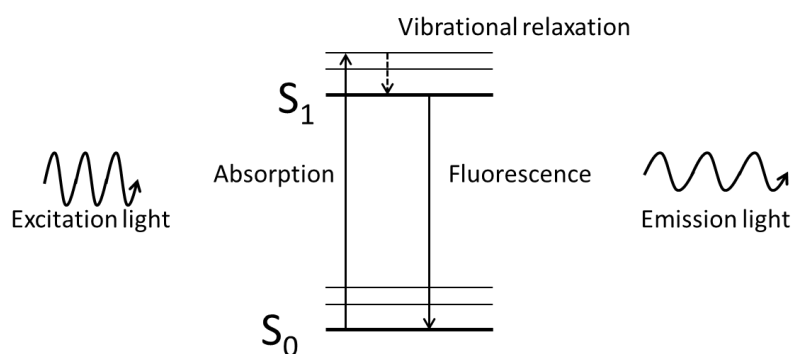


**Figure 17 A simplified Jablonski diagram.** This diagram depicts the creation of fluorescence photons involving two electronic states: ground state $S_0$ and the first excited state $S_1$. The thinner lines above the electronic states are vibration levels with higher energy.

When an excitation light of higher energy (shorter wavelength) is absorbed by the fluorophore, the dye is excited from the ground state $S_0$ to a higher vibrational level of the first excited singlet state $S_1$ (Figure 17). The fluorophore will eventually lose energy and relax to the lowest vibrational levels of $S_1$ through collisions: a process called vibrational relaxation. The

fluorophore will return to the ground state by emitting a light with lower energy (longer wavelength). The entire shift of fluorescence emission spectra to the longer wavelength side is termed Stokes shift. Since the fluorescence phenomenon normally occurs in a timescale around 1 ns to 100 ns, the measurements done throughout this project were steady state measurements.

The fluorescence intensity is directly depending on the quantum yield of the fluorophores selected. The intensity is also linearly proportional to the concentration when the absorbance is less than 0.05, due to inner filter effect (*100–102*). The three dyes selected were FAM, TYE and CY5 that have molar absorptivity of 75 000, 137 800 and 250 000 at maximum absorbance, respectively. With path length of the cuvette as 1 cm, the maximum concentration that still satisfies the linearity is 2 μM.

The 5' ends of DNA nanomotor's legs are attached with BHQ-1 quencher and the 3' ends of the binding sites of the DNA duplex track are attached with dyes. Movement could then be determined by measuring quenching percentage of these dyes while irradiation operation is performed on the motor-track sample. For example, after cycles of irradiation operation, if the nanomotor moves to the end of the track (plus-end), a decrease of fluorescent signal of the fluorophore attached to the plus-end binding site is expected. For motor version II, three dyes were attached on the track, giving more information of the movement of nanomotors from the beginning to the end of the track. These were ensemble measurements and the signal is an average of

possible nanomotors' movement with different starting state. Therefore, the actual performance of the nanomotors is expected to be better.

The cuvette was rinsed with ethanol for at least three times followed by ten times of ultrapure water. The track sample was diluted with suitable buffer such that no air gap is present for the path of incident light beam. Kinetic mode/time measurement was selected to measure fluorescent intensity against time and performs irradiation operation at the same time. For each round of irradiation operation, the motor-track sample was first irradiated by visible light for a defined duration followed by another period of UV irradiation. The wavelengths selected during visible light operation were to match the excitation wavelengths of the dyes such that fluorescence measurement could be collected.

# Chapter 3   Motor Version I

## 3.1   Modular motor

The four regimes discussed in section 2.2 allow the construction of nanomotors with functionally and spatially separable 'wheels' and 'engines': the former are a pair of identical legs asymmetrical bound with the track; the latter are a bi-state switch that changes between two values of length. Such a modular design is implemented in a light-powered DNA nanomotor, which is schematically illustrated in Figure 18.
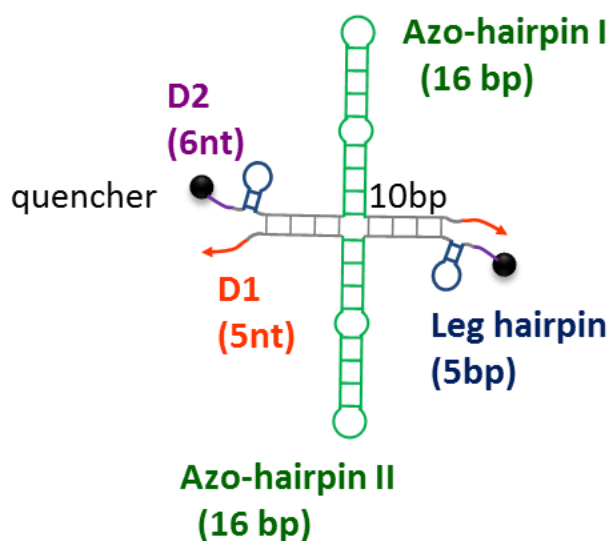


**Figure 18 First version of light-driven motor.** The winding hairpins consist of twelve azobenzene moities tethered to the nucleotides as side chains in the hairpin stem. The bulge loop is to ease the opening of the azobenzene hairpins. The two different legs D1 and D2 binds to D1* and D2* of one composite binding site on the track. The smaller leg hairpin (blue) is the hairpin on the legs that provide the necessary length during contraction of the motor.

The motor has two pairs of identical legs connected by a light-switchable four-way junction. This junction consists of two engine-like hairpins tethered with light-responsive azobenzene and two body duplexes separating the engine and the legs. The stem sequence for one hairpin has been modified to be parallel to the other hairpin such that it prevents the two hairpins hybridize to form irreversible duplex. Alternating visible light and UV irradiations close and open the hairpins, thereby resulting a contraction and extension of the motor like the piston of a car engine. The sequence for the two 8-bp-long stems of one hairpin is taken from a previously demonstrated hairpin (section 2.3). The smaller leg hairpins would be opened before the legs were detached from the binding sites during the contraction of the winding hairpins. They serve as another length provider to satisfy the geometry constraints. A quencher is attached to each of the 5' end of D2. If D2 leg hybridized with D2* of the binding site, the quencher will be in close contact with the dye on the binding site, greatly reducing the fluorescent intensity emitted.

The sequences for the motor are divided into segments and labelled according to their function. D1 and D2 are the motor legs that bind to D1* and D2* of a composite binding site, respectively. L1, LHP and L1* forms a leg hairpin that has a 5 bp stem. S1, S2, and S3 are the spacers necessary to satisfy the geometrical constraints discussed in the next section. WHP is the winding hairpin with 12 azobenzene moieties (labelled as X). B1 and B2 allow two motor strands (MS1 and MS2) to join together, forming the motor duplex.

| | |
|---|---|
| MS1<br><br>(97 nt+12X) | **BHQ1-D2-S2-L1-LHP-L1\*-S3-B1-WHP-B2-S1a-D1**<br><br>BHQ1-CCGTGA-TT-GTAGT-GGAATG-ACTAC-CA-<br><br>ATGGACGATC-<br><br>CTXTTXAAXGA(TTT)CTXTTXAAXGA(TTTT)TXCTXTAXAAG(T<br><br>TT)TXCTXTAXAAG-CGCATGCTAG-ATGT-CGCCT |
| MS2<br><br>(97 nt+12X) | **BHQ1-D2-S2-L1-LHP-L1\*-S3-B2\*-WHP-B1\*-S1a-D1**<br><br>BHQ1-CCGTGA-TT-GTAGT-GGAATG-ACTAC-CA-<br><br>CTAGCATGCG-<br><br>GAAXATXTCXT(TTT)GAAXATXTCXT(TTTT)AGXAAXTTXTC(T<br><br>TT)AGXAAXTTXTC-GATCGTCCAT-ATGT-CGCCT |

**Table 2 Sequences for motor version I.** The sequences of the two motor strands used to form the nanomotor are given in segments categorized by their function. X represents the azobenzene moieties and brackets mark the bulge and loop sequences of the winding hairpins. Asterisk marks complementary sequences.

## 3.2  Three-binding-site track
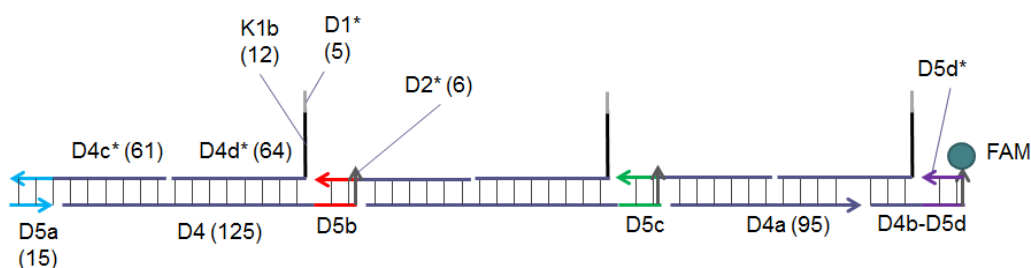


**Figure 19 Three-binding-site track.** The full track is comprises of three track units, with each unit holding two reconigtion part D1\* and D2\* for the hybridization with the motor legs. These two recognition sites form a composite binding site. Nicks are introduced between D4c\* and D4d\* to ease the technical difficulty of DNA annealing. K1b do not hybridize with any other strand by design and serves to provide necessary length for motor bindings. D5 is 15 nt part that joins the track units together.

| | |
|---|---|
| D4 (125) | CAATCATTAACGGTACGCCCTTGTTTGGGTTGATCGTTGGTAATTGTGA GGGGTAGGCAGGCTTCTTGGATAAAACCACCGAACTAATCGAGCGAAAT TCGTGCTGTAGTGTATCACCCTAGAAC |
| D4a (95) | CAATCATTAACGGTACGCCCTTGTTTGGGTTGATCGTTGGTAATTGTGA GGGGTAGGCAGGCTTCTTGGATAAAACCACCGAACTAATCGAGCGA |
| D4b (30) | AATTCGTGCTGTAGTGTATCACCCTAGAAC |
| D4c* (61) | CCTGCCTACCCCTCACAATTACCAACGATCAACCCAAACAAGGGCGTAC CGTTAATGATTG |
| D4d* (64) | GTTCTAGGGTGATACACTACAGCACGAATTTCGCTCGATTAGTTCGGTG GTTTTATCCAAGAAG |
| S1b (12) | CTTAAACTGACT |
| D1* (5) | AGGCG |
| D2* (6) | TCACGG |
| D5a (15) | CTGGAAAAAGGTGTG |
| D5b (15) | AGCGATTACTTGTGC |
| D5c (15) | CGGCGGGTCATCTAG |
| D5d (15) | TCTCTTATATCTGTG |

**Table 3 Track sequences of motor version I.** The sequences of the track are given in segment with labelling given in Figure 19. The numeral in the bracket indicates the number of nucleotides.

The track supporting three units are made of ten unique strands. Each unit is a duplex with two sticking ends that constitute one composite binding site (D1* and D2*); part of the sticky end (D5) join one track unit with another. With four unique sequences of D5 (D5a, D5b, D5c, and D5d), the FAM dye could be specifically arranged at the end of the track (plus end). The composite binding sites are separated from each other in an equal interval of

125 bp (D4 duplex). For the last track unit, D4b is separated from D4a instead of a long D4 duplex because of the technical requirement of attaching FAM dye. The track fabrication involved annealing of a long duplex (125 bp) with sticking ends is difficult; thus, nicks are introduced at D4*, breaking it to two strands D4c* and D4d*, to reduce the length of the annealing strand. Following ref. (*103*), the nicks do not affect the bending flexibility of a double-strand DNA shorter than the persistence length (50 nm). The separation of nearest composite binding sites (125 bp × 0.34 nm = 42.5 nm) is still less than the persistence length of double-strand DNA (50 nm), and thus is expected not to affect the motion much.

## 3.3   Motor operation mechanism

The D1 and D2 legs of the motor hybridize with the 17 nt D1* and the 6 nt D2* sticky ends, respectively, with the latter located closer to the track's plus end. In this state, both the winding hairpin and the leg hairpin are relaxed and in closed states (Figure 20 panel i). This motor only binds to one composite binding site, as the closed hairpins does not have enough length to span across two binding sites. Under visible light condition (duration of 10 minutes), the motor length (equivalent to 26 bp excluding the binding legs) is insufficient to bind across two composite binding sites (125 bp apart), thus only one of the motor legs binds to D1* and D2* part of one composite site. The overall power of the light source (for UV and visible light) is measured to be about 100 µW, and with the illumination area of about 1 cm$^2$, this gives intensity of 1 W/m$^2$.
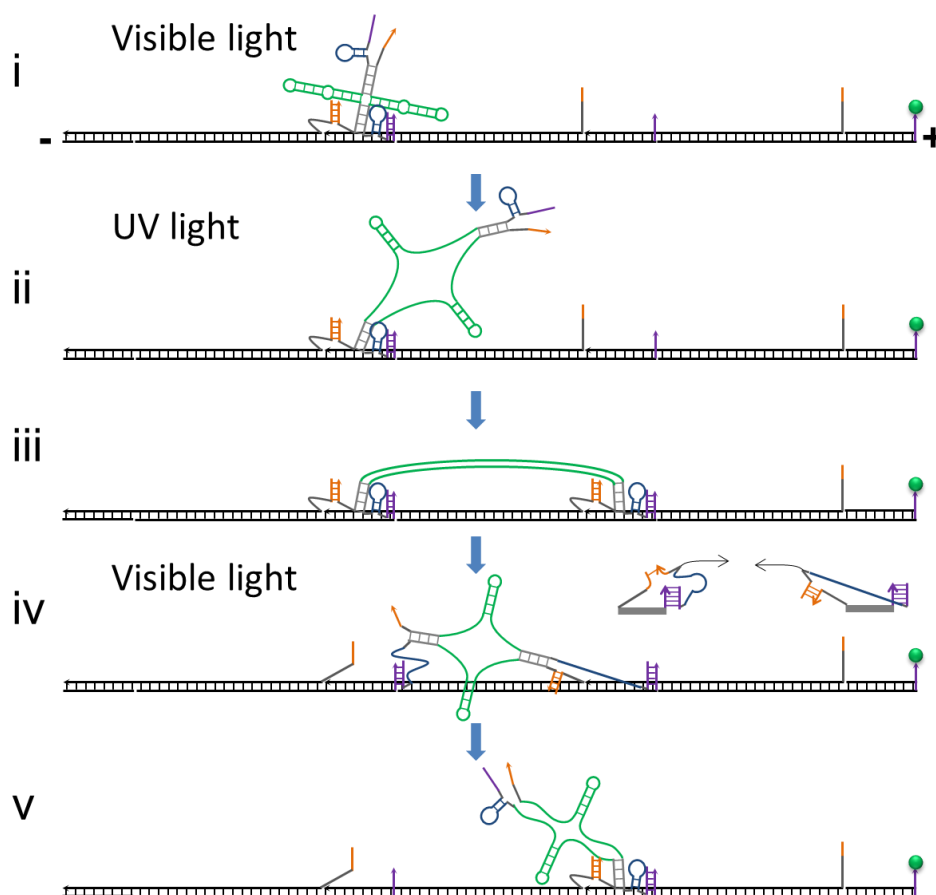
**Figure 20 Operation mechanism of motor version I.** Possible states of the DNA motor under alternating visible and UV irradiation. States ii-v may be matched to states C2, B2, B1 and C1 of regime R3 in Figure 15. (States ii and iii for expulsive mode and state iv and v for contracted mode). The inset illustrates the motor's rear and front legs under opposite pulling by the winding hairpins.

During the 30 minutes UV-light irradiation (panel ii), the winding hairpins will be extended from a close state with about 2 nm width to double strands equivalent to 54 nt (one hairpin is 42 nt long with an extra 12 azobenzene moieties, which can be treated as extra bases (*104*)). Compensating the motor body duplexes (B1 and B2) with the track duplex, the required motor length to bind across two composite binding sites is equivalent to 105 bp. The hairpins open to an unconventional double-strand DNA structure of unknown extension, but estimation can be made. The width of a closed leg hairpin

(about 3 nt), single-strand spacers (20 nt) and the opened winding hairpins gives 77 nt in length. If 1 bp and 1 nt are taken as 0.34 nm and 0.7 nm, respectively, the opened motor duplex has sufficient length to reach the forward composite binding site (panel iii). In the event of the motor's legs initiated hybridization with the forward composite binding site, the unconventional double-strand DNA structure is expected to be fairly stretched because of the length of the D4 duplex.

Re-application of visible light irradiation will again stabilize formation of the winding hairpins. The hairpins will rewind and generate a force to break the motor-track bindings. Initially, the leg hairpins will be opened by this winding force (panel iv). When the rear legs were pulled, both D1* and D2* leg components will be pulled. For D2*, the force will be used to open the leg hairpin; for D1*, the duplex formation between the leg and binding site will be broken (inset). In the meantime, the leg hairpin is fully open and for the front leg, both legs meet at the same point to the motor body duplex. The distances from the duplex body (B1-B1*) to the binding parts are designed to ensure that they shared the winding force equally, and compete with the rear leg that only has one part resisting force due to difference in length. The front legs will share the force, and act against the lone D1* of the rear legs. Thus, D1-D1* duplex of the rear leg will be the first to break. The winding continues until the D2 of the rear leg is detached from D2* as well.

When the rear leg is fully detached, the tension is relaxed and the leg hairpins (blue hairpins in Figure 20) reform as well. During this reformation,

the D2 part of the front leg became shorter than the D1 part (Figure 21), effectively pulling the motor forward, giving it a power stroke. The motor regains the single-binding state and made a step. Visible-light and UV cycle can be repeated for more steps. Eventually, all motors will move from the minus end to the plus end.
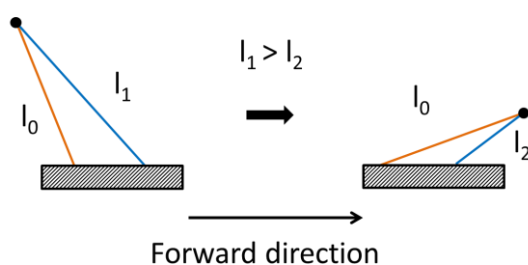


**Figure 21 The forward bias.** The orange and blue lines correspond to D1 and D2 motor leg with leg hairpin, respectively. If the leg hairpin reforms, the end-to-end distance will decrease but the leg of D1 maintains: this will introduce a swinging motion forward.

## 3.4   Materials and methods

### 3.4.1   Geometrical constraints

The first step for a successful motor movement cycle was calculating the geometrical constraints necessary for each state of the motor movement. Two important parameters used in determining the length requirements are the duplex length unit, base pair (bp), and the single strand length unit, nucleotide (nt). 1 bp and 1 nt were taken as 0.34 nm and 0.7 nm, respectively. The boundary conditions of the geometrical constraints are as follow:

Under UV irradiation, the winding hairpin opens and the motor must have enough length to cover two composite binding sites. Let l and d represent the length of a single strand DNA and duplex, respectively, and $l_{OM}$ be the length of the extended motor body when the winding hairpin is fully open, which is equals to $0.34(d_{B1}+d_{B2}) + 0.7l_{WHP}$. The minimum $l_{OM}$ would have to satisfy the inequality:

$$l_{OM} + 0.7(l_{S1} + l_{S2} + l_{S3}) + 2 > 0.34\gamma(2d_{D5} + d_{D4}) \qquad (2)$$

The additional 2 nm term on the left-hand side of the equation refers to the width of a closed leg hairpin. $\gamma$ is the adjustment factor included to give clue to the flexibility for the design, and a value of 1.07 was used. A few starting lengths for the leg hairpins and the track's binding sites were fixed with consideration to minimize the overall length of the track. The parameter was then obtained by further adjusting the length of other components. It measured how well the system fits the geometrical constraints rather than was chosen deliberately.

Ratchet requires the selection dissociation of the rear leg when both front and rear legs are subjected to the same tension from the winding hairpin. Therefore, the distances from the duplex body (B1-B1*) to both front leg parts should ensure that they shared the winding force equally. In other words, the length of fully opened D2*-containing leg parts should covered the distance between two leg parts and the spacer (S1) that connects D1* and the duplex body, giving:

$$0.7(l_{S2} + l_{S3} + l_{L1} + l_{LL} + l_{L1^*}) = 0.34d_{D5} + 0.7l_{S1} \tag{3}$$

This is used to determine the minimum length for the spacers. Meanwhile, the rear leg should break part by part. This can be achieved by first fully stretching the rear leg part that contains the D1-D1* pair, while the D2-D2* pair remained fairly relaxed. Thus, the length of the D2* leg part should be longer than the D1* leg part:

$$0.34d_{D5} + 0.7(l_{S2} + l_{S3} + l_{L1} + l_{LL} + l_{L1^*}) > 0.7(2l_{D1} + l_{S1}) \tag{4}$$

The factor 2 in the $l_{D1}$ term corresponds to the requirement of D1-D1* is fully detached from each other. After the preferred D1-D1* pair is broken, the subsequent D2-D2* breaking can be achieved by limiting its length to be less than the distance between two composite sites when the winding hairpin is close:

$$\begin{aligned}0.7(2l_{D2} + l_{S1}) + 0.7(l_{S2} + l_{S3} + l_{L1} + l_{LL} + l_{L1} *) + \\ 0.34(2d_{B1}) + 2 < 0.34\, l_{D4}\end{aligned} \tag{5}$$

This determines the minimum length of D4, such that it is longer than the length of the motor in its closed state.

Power stroke is achieved in this motor by having a shorter D2* leg part, as compared to D1* leg part, when the hairpins are in closed state, effectively tilting the motor closer to the forward binding site. Ideally, the length of D2* leg part in closed leg hairpin state, $0.7(l_{S2}+l_{S3}) + 2$ should be less than half of

the distance between two binding legs ($l_{D5}$) but it is not possible due to leg hairpin width. Therefore, a compromise must be made. When the tension is released, the leg hairpin should reform and the length of the leg part that has D2* should be shorter than leg part that has D1*:

$$0.7 l_{S1} > \delta[0.34 l_{D5} + 0.7(l_{S2} + l_{S3}) + 2] \tag{6}$$

$\delta$ is the adjustment factor and obtained in a similar way to $\gamma$, a value of 1.13 was used.

| $d_{B1}=d_{B2}$ | 10 | $d_{D5}$ | 15 |
|---|---|---|---|
| $l_{S1}$ | 16 | $l_{L1}= l_{L2}$ | 5 |
| $l_{S2}$ | 2 | $l_{LHP}$ | 6 |
| $l_{S3}$ | 2 | $l_{D1}$ | 5 |
| $d_{D4}$ | 125 | $l_{D2}$ | 6 |

**Table 4 Length parameters used considering the geometrical constraints.** The above conditions led to limited parameters for the length of different components of the motor and track. Some values were pre-fixed to ensure stability of the motor and track, such as $d_{B1}$, $d_{B2}$ and $d_{D5}$. The length of S1 was split to two parts as S1a and S1b, reducing the technical difficulty of the motor fabrication.

With the geometrical constraints considered, the possibility of formation of motor was tested using NUPACK (*93*), and it is expected to form under equilibrium at 25°C (Figure 22).

MFE structure at 25.0 C

Free energy of secondary structure: -63.88 kcal/mol
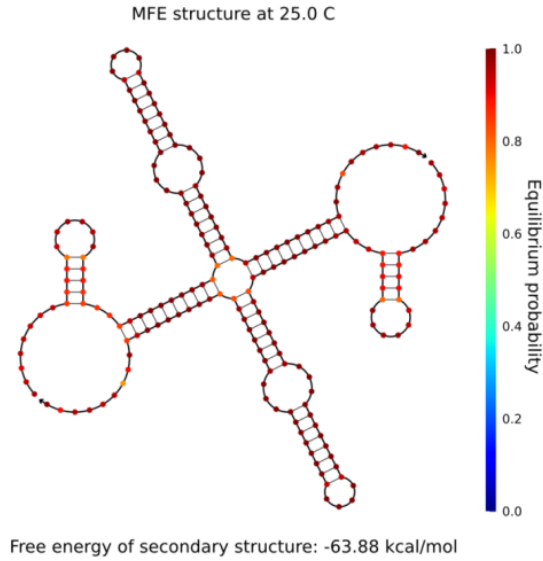
**Figure 22 Prediction of formation of motor using NUPACK.** The structure formed matches the design at 25°C.

### 3.4.2 Motor-track configuration energy

The motor operation was further tested by determining the configuration energy of the track-nanomotor binding combinations. This is to verify that the motor operation follows an energy favourable path to achieve the next step. Configuration energy for nanomotor and track is determined using the following equation (*105*):

$$E_C = F_H + n_{D1}U_{D1} + n_{D2}U_{D2} + n_{LHP}U_{LHP} + n_{WHP}U_{WHP} \tag{7}$$

The first term at the right hand side of the equation refers to the Helmholtz free energy from the worm-like chain model (*106*) to account for stretching energy of single-strand portion of DNA motor, and the last four terms are binding energies of the D1 and D2 legs, the leg hairpin, and the winding hairpin, respectively (Figure 23). Following ref. (*36*), the Helmholtz free

55

energy (equation 8) can be obtained by integrating the force term given in the worm-like chain model (*106*) from zero extension to the distance between two binding sites to give:

$$F_H = k_B T \left(\frac{l_e}{l_p}\right)\left[\frac{\left(\frac{d_e}{l_e}\right)^2 \left(3 - \frac{2d_e}{l_e}\right)}{4\left(1 - \frac{d_e}{l_e}\right)}\right] \tag{8}$$

where $l_e$ is the stretchable single-strand portion of the nanomotor, $d_e$ is the effective length on the track for stretching of the nanomotor and $l_p$ is the persistence length of single strand DNA (taken as 1 nm), respectively. The motor was treated as lying close to the track. $l_e$ is calculated by subtracting all the non-stretchable duplex on the motor. Depending on the motor's binding to the track, the distance d between binding sites together was subtracted with the distance-occupying body duplex B1 and B2, and width of the hairpin stem, $w_{duplex}$: $d_e = d - (d_{B1} + d_{B2}) - n_{duplex}w_{duplex}$, where $n_{duplex}$ denotes the number of hairpins in the calculation.

The track-nanomotor configuration energy is calculated for different possible states. These estimated energies provide a rough guideline to select the motor's length with respect to the binding sites period according to relative stability of motor-track binding states. Nevertheless, a quantitative link between the estimated configuration energies and the motor's performance has been difficult to establish. A previous attempt on another DNA nanomotor (*31*) turned out unsatisfactory for quantitative agreement due to the difficulty to model complex dynamic DNA systems in a realistic way. Therefore, the

estimated numbers for the configuration energies for this motor were not
elaborated on deliberately to avoid misleading statements.
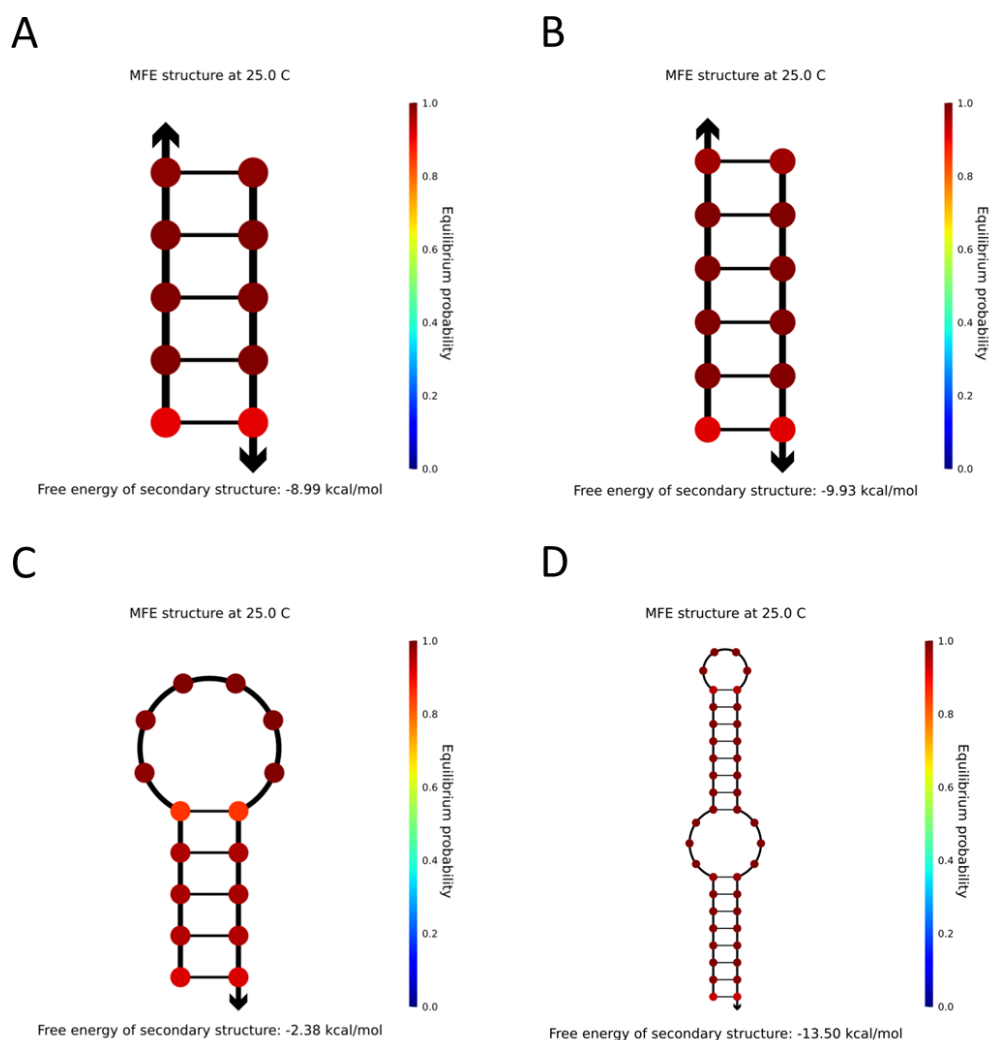


**Figure 23 Free energies of different parts of motor-track at 25°C.** The free
energies were determined using NUPACK. A. The binding of the motor leg D1
and the track binding site D1*. B. The binding of the other leg and the binding
site D2-D2*. C. The leg hairpin is weaker than both the motor-track leg
binding by design. D. The winding hairpin without inclusion of azobenzenes.
Azobenzene does not disrupt the stability of the winding hairpin; thus it is safe
to assume that this structure resembles the actual winding hairpin with
azobenzenes.

### 3.4.3 Motor-track assembly

The motor and individual track units were mixed stoichiometrically and annealed at 95°C for 5 minutes and cooled down to 25°C in water bath, and finally stored at 4°C. The full three-binding-site track was then formed by annealing the three track units together at 70°C for 40 minutes, followed by cooling to 27°C in water bath, and finally stored at 4°C. The annealing buffer used was 40 mM Tris (pH 8.0), 20 mM acetic acid, 2 mM EDTA and 12.5 mM magnesium acetate.

6% native polyacrylamide gel (PAGE), suitable for separation range of 60-80 bp to 400-500 bp, was used to analyse the track formation. The gel was run at 60 V for 100 minutes in 1× TBE buffer. Sybr Gold (excitation wavelength of 300/495 nm and emission wavelength of 537 nm) was then used to stain the gel. The gel was imaged using Blue Sample Tray in a Bio-Rad Gel Doc EZ System.

### 3.4.4 Verification of azobenzene-tethered hairpins

To visualize the presence of the incorporation of azobenzene moieties in the motor strand, a 133 nM of motor was prepared with TAE buffer, and checked with a Shimadzu UV-1800 spectrometer (Figure 24). The absorption measurement was run against a TAE buffer background.
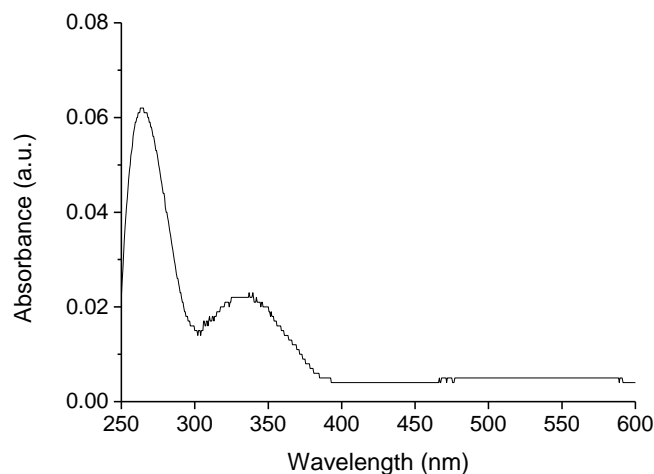
**Figure 24 UV-visible absorbance spectra of azobenzene-tethered motor duplex.** Two peaks were found at around 260 nm and 330 nm. Absorbance peak at 260 nm is typical for DNA. The 330 nm peak is consistent with the presence of azobenzene (section 1.5).

### 3.4.5 Motility measurement

An equimolar mix of the motor and track sample was incubated over 12 hours to ensure that the motor-track binding achieves thermodynamic equilibrium. The final concentration of the sample is 50 nM (diluted with 12.5 mM magnesium acetate, 40 mM Tris, 20 mM acetic acid 2 mM EDTA buffer) to suppress possible cross-linking of one motor across two tracks. Even though cross-linking still can happen in the time frame of the experiment, the motor's motion across two nearby tracks is likely random due to random orientation of the tracks. Thus, it does not change the conclusion on the directional movement of the motor; rather it might reduce the performance of the motor. Thus, the signal obtained likely underestimated the motor's performance. The

incubated sample was then used for light operation and fluorescence measurement.

The motor's motion under the irradiation operation was monitored by detecting the quenching of the fluorescence signal of FAM dye, which is tethered to the plus-end track binding site. The motility experiments were conducted using a Cary Eclipse spectrophotometer (75 kW peak power Xenon flash lamp) at 10°C and 25°C. For each round of irradiation operation, the motor-track sample was first irradiated by visible light (excitation wavelength of the FAM dye: 495 nm with 5 nm slit width) for 10 minutes, followed by another 30 minutes of UV irradiation (350 nm with 5 nm slit width). The fluorescence was collected during the visible irradiation time.

Before initiating the light operation, the pre-mixed motor and track complex was cool down to 10°C from 25°C using a attached peltier with a ice bath. The ice bath was replenished from time to time. The final temperature could be reached within 15 minutes and the sample was kept at 10°C for a total of 210 minutes. The fluorescent intensity was decreasing during the cooling period as lower temperature could probably promote more radiationless relaxation. The operation experiment was started after the decrease was stabilizied when the motor-track sample was re-equilibrated.

## 3.5 Results and discussions

### 3.5.1 Motor-track formation

The gel analysis of the annealed products yields one prominent band that is identified as the assembled motor and track (Figure 25).
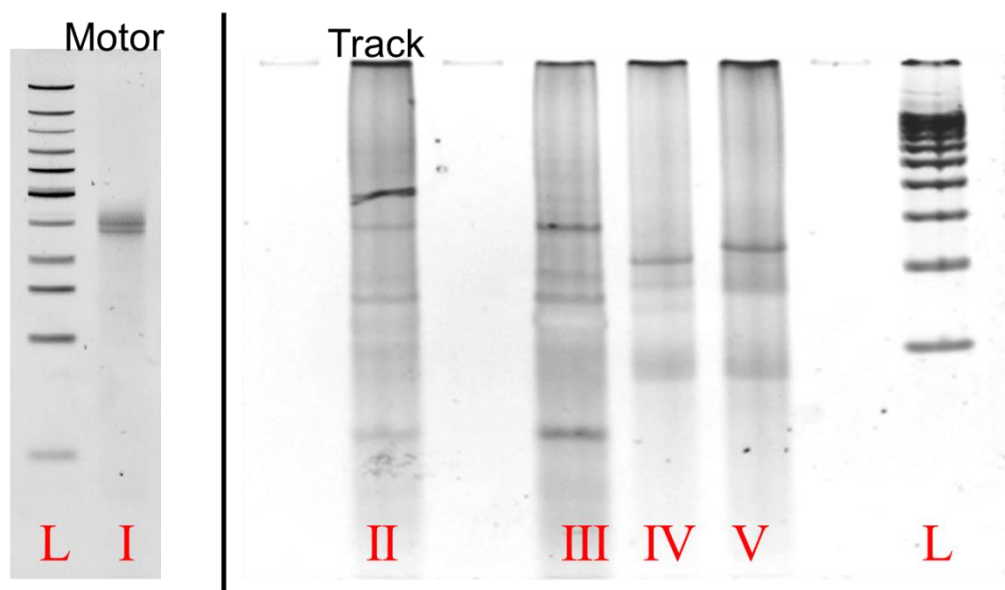


**Figure 25 The motor and track fabrication.** Shown are gel images obtained using native PAGE (Polyacrylamide gel electrophoresis). The left lane L is a low molecular weight DNA ladder (purchased from New England BioLabs Inc., with 25 bp and 766 bp as the lowest and highest band); the right lane L is a GeneRuler 100 bp DNA Ladder (purchased from Thermo Fisher Scientific Inc., with 100 bp and 1000 bp as the lowest and highest band). Lanes III, IV and V are the three annealed track units required for a full track. Lane II shows the band for a full track.

### 3.5.2 Low temperature operation

Three motor-track samples were operated at 10°C for 15, 20 and 23 cycles (Figure 26). Two control experiments were also done using either long UV or long visible light. The motor-track sample in the long UV control was irradiated at 350 nm for 760 minutes and fluorescence was observed at the end.

61

A long UV control corresponds to one cycle of light operation with extended duration of UV light irradiation. Similarly, a long visible control means that the sample was monitored continuously with an excitation wavelength of 495 nm. In other words, the long visible control is to observe the effect of photobleaching. The three light-operated motor-track samples exhibit fluorescent signals that were lower than the two controls, indicating that the drop of fluorescence was not due to mere photobleaching, but was induced by directional motion of the motor under alternate light operation. The drop varies from 40% to 90%, which could be attributed to difference in population of motor-track bindings available. The flattening of signals for sample 2 and 3 at the end indicates that there is no more motor coming from the minus end to the plus end. The observation of motor's directed motility at low temperature supported the prediction, by NUPACK free energy calculation, of low population (about 2%) of motor-track bindings.
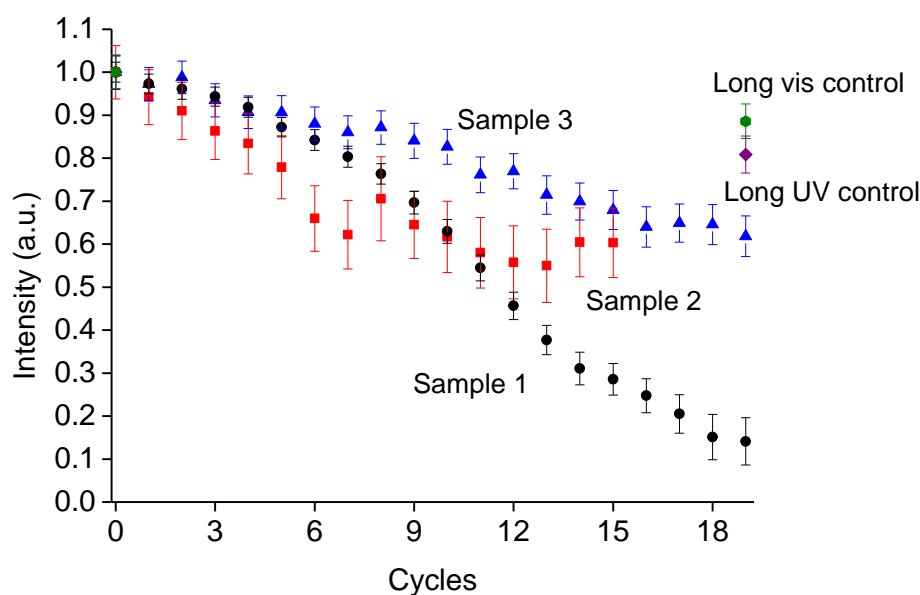
**Figure 26 Motor operation and controls.** The samples were operated for at least 15 cycles or 10 hours with 10 min visible and 30 min UV light operation. The controls show that the motor indeed moves to the end of the track.

### 3.5.3 Room temperature operation

The intensity remains unchanged after seven cycles of light operation for two motor-track samples were conducted at 25°C (Figure 27A). The disparity in the experimental results for 10°C and 25°C is most likely due to the motor not binding to the track at room temperature. It is expected that the motor-track binding is better at lower temperature and reduces the possibility of complete derailment of motor from the track; therefore, giving larger fluorescent signal drop. Although the length of binding site is the same for motor operations at both temperatures, short length (5 bp) would discourage motor-track binding at higher temperature due to thermal fluctuation.

### 3.5.4 Salt concentration

Another possible factor that could promote binding between motor and track is salt concentration that provides positive charges to compensate the negatively-charged the DNA structure, increasing the probability of motor and track bindings. The fluorescent signal at 100 mM NaCl is shown in Figure 27B gives no reduction of the fluorescent signal expected for motor movement. Since the motor-track sample was later successful at low temperature, the seeking of workable salt concentration was not continued.
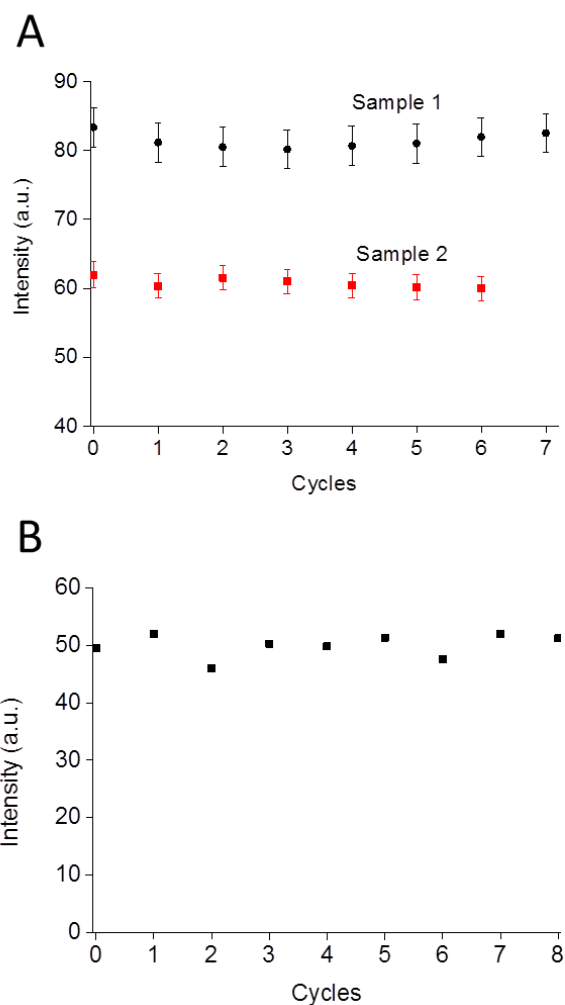
**Figure 27 Track-motor operation with different parameters.** A. Fluorescent signal of motor operation at 25°C. B. Fluorescent signal of motor operation with 100mM NaCl added to the track and motor complex. There is no sign of reduction of the fluorescent signal of FAM dye at the end of the track, suggesting at room temperature and even the addition of salt concentration is not enough for successful binding and motor movement.

## 3.6   Conclusion

The first version of nanomotors following the modular design with optical switching was demonstrated to move directionally along a three-binding-site track. Geometrical constraints and motor-track configuration energy were calculated to guide the design of the nanomotor. Various verifications were

then performed to ensure the formation of motor and track. Comparing the motor's operation against experimental controls, we can conclude that the nanomotor moved to the plus end of the track at low temperature of 10°C. It was suspected that the binding site was too short to allow a stable motor-track binding at room temperature, even though the concentration of salt was increased.

# Chapter 4   Motor Version II

## 4.1   Motor with modified legs
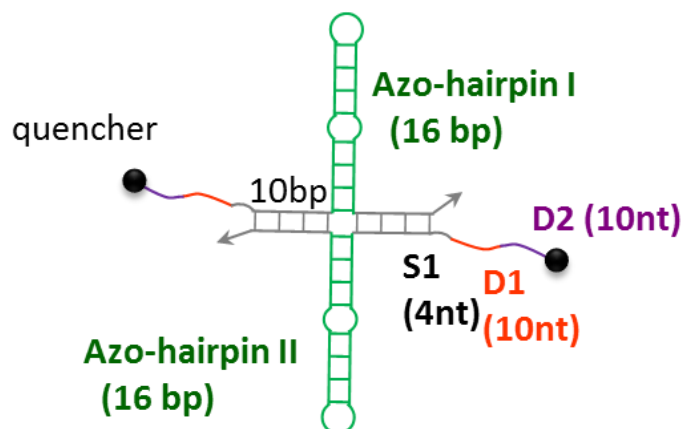


**Figure 28 Second version of light-driven motor.** The motor is made of the same engine as the first version, but with different leg configuration. The motor is labelled with quenchers (BHQ-1) for characterization.

Similar to motor version I, the second motor has two identical single-stranded legs connected by the same light-switchable four-way junction. The difference is the leg that is made of two segments, D1 and D2. The two-segment leg binds to one composite binding site of the track competitively. A quencher (BHQ1) is attached to each of the 5'end of the motor's leg.

The motor is made of two 97 bp strands, MS1 and MS2. The strands each contain a 20 nt two-segment leg (D2-D1), a 42 nt hairpin embedded with 12 azobenzene moieties in the nucleotide backbone, two 10 nt double-strand spacers (B1, B2) for separating the leg and hairpin, and three linker segments (S1, S2, S3 of 4, 9 and 2 nt, respectively) for flexibility (Table 5).

| MS1 (97 nt + 12 X) | **BHQ1-S3-D2-D1-S1-B1-H1-B2-S2**<br><br>BHQ1-CC-GTGATTGTAG-TGGAATGACT-ACCA-<br><br>ATGGACGATC-<br><br>CTXTTXAAXGA(TTT)CTXTTXAAXGA(TTTT)TXCTXTAXAAG<br><br>(TTT)TXCTXTAXAAG-CGCATGCTAG-ATGTCGCCT |
|---|---|
| MS2 (97 nt + 12 X) | **BHQ1-S3-D2-D1-S1-B2\*-H2-B1\*-S2**<br><br>BHQ1-CC-GTGATTGTAG-TGGAATGACT-ACCA-<br><br>CTAGCATGCG-<br><br>GAAXATXTCXT(TTT)GAAXATXTCXT(TTTT)AGXAAXTTXTC<br><br>(TTT)AGXAAXTTXTC-GATCGTCCAT-ATGTCGCCT |

**Table 5 Sequences for motor version II.** The sequences are given in segments categorized by their function. X represents the azobenzene moieties and brackets mark the bulge and loop sequences of the winding hairpins. Asterisk marks complementary sequences.

## 4.2 Three-binding-site track with three dyes
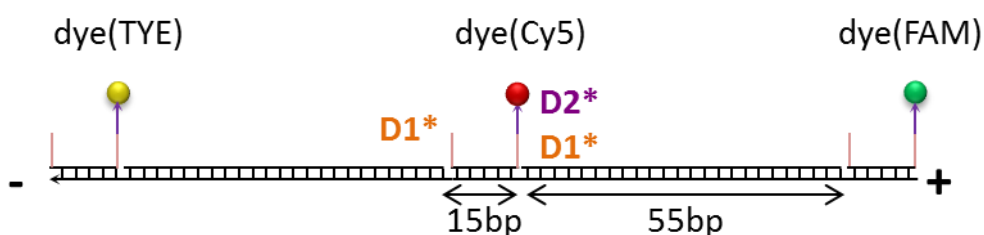


**Figure 29 Three-binding-site track for the motor version II.** The track has a periodicity of 70 bp and could accommodate up to two steps for the motor. TYE, CY5 and FAM dye-carrying strands are designated as the minus-end site, middle and plus-end site, respectively. D1*, D2* in the binding sites are complementary sequences to the leg sequences D1, D2.

The three-site track (Figure 29) is made of three strands for binding sites (TS1, TS2, TS3, 45 bp each, carrying dyes TYE, CY5 and FAM, respectively), two identical spacer strands (TS4, 55 bp) and a long template (TS5, 155 bp). The composite binding sites are identical, and each contains two sticky ends for leg binding. Below are the sequences for the strands:

| TS1 (45) | D1*-B3*-D1*-D2*+TYE<br><br>(B3* = CAACAGCAATGTTCG) |
|---|---|
| TS2 (45) | D1*-B4*-D1*-D2*+CY5<br><br>(B4* = TTACAATCCGTCGTG) |
| TS3 (45) | D1*-B5*-D1*-D2*+FAM<br><br>(B5* = AGCGATTACTTGTGC ) |
| TS4 (55) | B6* = AGCTAGTCCAAGGGGATCGTAGTATTTTGCATGACAAAGC<br><br>CCCAGCCATTATAGC |
| TS5 (155) | B5-B6-B4-B6-B3 |

**Table 6 Track sequences for motor version II.** The sequences of the track are given in segment (from 5' end to 3' end). The numeral in the bracket indicates the number of nucleotides.

The two-site tracks were made to test dissociation and directional bias. Three short templates truncated from TS5 as B5-B6-B4, B5-B6-B3 and B4-B6-B3 were used. The resultant tracks carry two dyes, namely TYE-CY5, TYE-FAM and CY5-FAM respectively, from minus to plus end.

## 4.3 Motor operation mechanism

The asymmetric binding comes from the design feature that the two adjacent sticky ends at a site: 10 nt D1* and 20 nt D2*-plus-D1*, with the latter leading towards the track's plus end (Figure 30). The two sticky ends compete to bind the motor's leg with complementary D1, D2 sequences. A leg may hybridize simultaneously with both sticky ends into D1-D1* and D2-D2* duplexes (both 10 bp long) as allowed by the length of the sticky ends. However, the duplex at the longer sticky end can grow to weaken the D1-D1* duplex at the shorter one. The D1-D1* weakening is decelerated or accelerated when the leg is pulled backward or forward, respectively, via its D1 segment linking to the motor's main body (inset). This gives rise to preferential rear dissociation when a visible irradiation closes both hairpins to shrink the motor into a contracted mode. The contracted mode subjects the rear leg to a forward pull to break its D1-D1* duplex preferentially (panel i). The remaining duplex is readily unzipped base-by-base by the motor's inward tension generated by the double-hairpin engine, while a simultaneous shearing of multiple base pairs is required to break the D1-D1* duplex at the front leg (panel ii). This process gives the asymmetry as the shearing force is higher than the unzipping force (more analysis given in section 1.4). Hence, the visible irradiation dissociates the rear leg preferentially (panel iii).
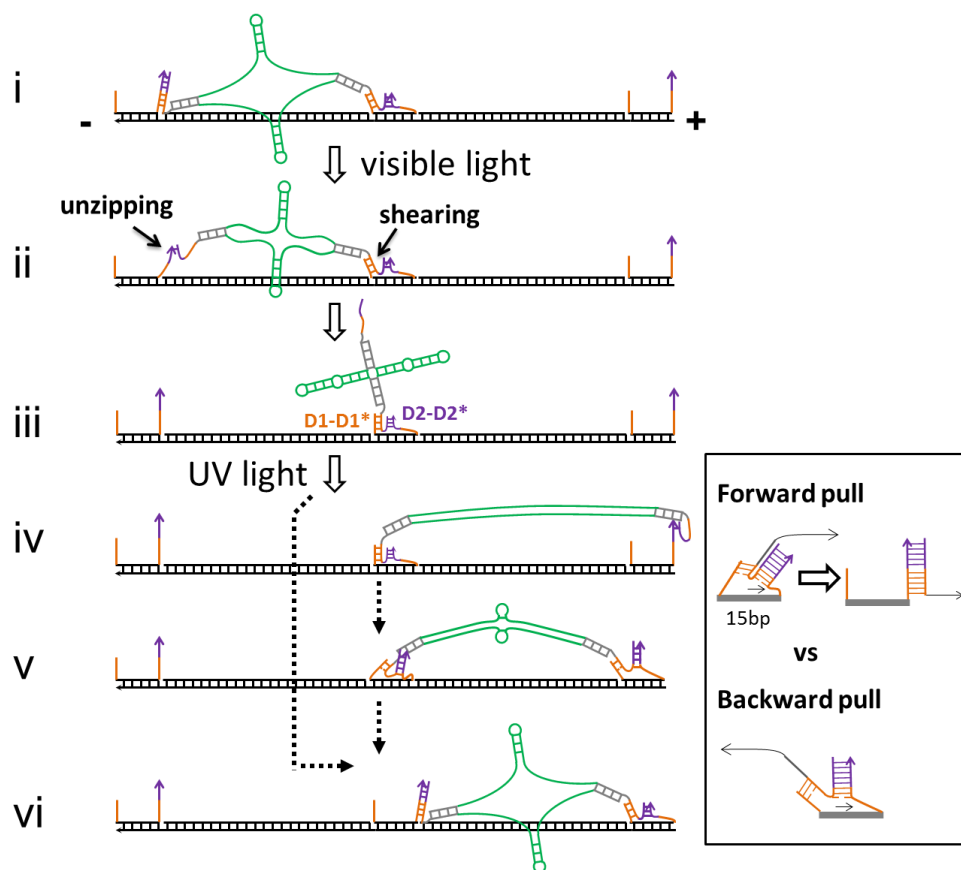
**Figure 30 Operation mechanism of motor version II on the three-site track.**
Possible states of the DNA motor under alternating visible and UV irradiation.
States ii-v may be matched to states B1, C1, C2, B2 of regime R3 in Figure 15
(states ii, iii for a contracted mode; iv, v for an expulsive mode). The inset
schematically illustrates the motor's rear and front legs under opposite pulling
by the winding hairpins. The rear leg is dissociated along the forward edge of
the binding site (corresponding to the less steep edge in Figure 15) and the
front leg along the backward edge (the steeper edge), hence preferential rear
leg dissociation.

An ensuing UV irradiation opens the two hairpins to release two anti-
parallel strands (each about 54 nt long, including 12 azobenzene moieties that
add to the backbone length similar to extra nucleotides (*104*)). With non-
complementary sequences the two strands cannot form a standard B-DNA
helix, but their close proximity may allow many hydrogen bonds to form,
likely leading to an unconventional DNA duplex of unknown extension
(probably longer than B-DNA helices). If the UV-switched engine reaches an

extension equivalent of about 2.5 turns of standard helices, the motor is near a relaxed mode for the dissociated leg to form the D2-D2* duplex at the front or back site. The motor then realizes regime R1 under repeated alternating visible-UV irradiations. If the engine reaches an extension equivalent of 4 helical turns or more, the motor's bridge (the opened hairpins plus two 10 bp spacers and two 4 nt linkers) is beyond the binding site period (70 bp). If the motor is so long that it bends to approach the back site from the outer, steeper edge for the D2-D2* duplex formation, the dissociated leg will bind the front site preferentially over the nearer back site (panels iv to v). The motor then accesses the expulsive mode, and realizes regime R3 under alternating visible-UV irradiations. A preferred forward binding is also possible if the track-bound leg is dragged forward to the less steep edge by the growing D2-D2* duplex (panel vi). Whether the motor can access R1 or a better regime depends on unknown size of an unconventional DNA structure, and can only be answered by experiments at this stage.

## 4.4   Materials and Methods

### 4.4.1  Motor-track assembly

All the track strands were mixed stoichiometrically in a buffer containing 1.5 M NaCl, 10 mM Tris, 1 mM EDTA buffer (pH 8). The mixed sample was annealed at 95°C for 20 minutes, and then cooled down to 25°C for over 4 hours, and finally stored at 4°C. The motor was assembled by the same annealing procedure in a similar buffer (2 M of NaCl instead).

The annealed products were analysed in a 10% native PAGE gel with reference to a low molecular weight DNA Ladder (New England BioLabs, Inc., with 25 bp and 766 bp as the lowest and highest band, respectively). The gel was run at 90 V for 70 minutes in 1×TBE buffer. Gel Red (Biotium Inc., with excitation wavelength of about 300 nm and emission wavelength near 600 nm) was used to stain the gel. The gel was imaged using UV Sample Tray in a Bio-Rad Gel Doc EZ system.

## 4.4.2  Motility measurement

The motor's motion under the irradiation operation was monitored by detecting the fluorescence of different dyes that are tethered to the track site-specifically and subject to quenching by the motor-carried quenchers. Incubated motor-track samples of equilibrated motor-track binding (verified by constant fluorescence) are used for the operation experiments so that the motor's motion towards the plus end is signalled by a dropping fluorescence from the plus-end dye and a concomitant rising fluorescence from the minus-end dye. Each operation experiment on a motor-track mix is accompanied by a control experiment in which the same irradiation operation is applied to an equal amount of bare tracks without any motor. The fluorescence of the operated motor-track mix divided by that of the bare tracks is the real signal for the motor's operation largely free of dye optics. Such a control-calibrated fluorescence yields reliable information on site occupation by the motor and its binding/dissociation preference by further exploiting the nearly 100% efficiency (*107*) of contact quenching for the present motor.

Similar to the motility measurement of the previous motor (section 3.4.5), the motor-track mix was incubated 12 hours before an operation experiment. Both the incubation and later operation were done at 25 °C in a buffer containing 15 mM sodium acetate, 9.5 mM Tris, 1 mM EDTA. The motor and track concentration was kept low (about 5 nM) for all the operation experiments to suppress possible cross-linking of multiple tracks by one motor.

The irradiation operation and fluorescence measurement were both done using a RF-5301PC spectrophotometer (150 W Xenon lamp, Shimadzu Corp.) For each round of irradiation operation, the motor-track sample was first irradiated by visible light for a defined duration (wavelengths of 495 nm, 549 nm, 648 nm over 5 nm slit width each) followed by another period of UV irradiation (360 nm over 5 nm slit width). The fluorescence was collected during the visible irradiation, which was also the excitation for the three dyes (excitation/emission wavelengths: 495 nm/520 nm for FAM, 549 nm/563 nm for TYE, 648 nm/668 nm for Cy5).

### 4.4.3   Occupation probability and rate ratios

The probability for site occupation by a motor is related to the fluorescence of the dye tethered to the site as (*31*)

$$P(t) = \frac{1}{\gamma}\left[1 - \frac{I_{MT}(t)}{I_T(t)}\right] = \frac{1 - I_M(t)}{\gamma} \tag{9}$$

74

$I_{MT}(t)$ is the fluorescence signal collected from an operated motor-track sample at a time t, and $I_T(t)$ is the fluorescence of an equal amount of bare tracks from the accompanying control experiment. $\gamma$ is the quenching efficiency of the dye by the motor-carried quencher. Hence the control-calibrated fluorescence $I_M(t) = I_{MT}(t)/I_T(t)$ yields the probability as above.

The average rate for leg dissociation from time $t_1$ to a later time $t_2$ is

$$k_d = \frac{P(t_1) - P(t_2)}{(t_2 - t_1)} = \frac{I_M(t_2) - I_M(t_1)}{\gamma(t_2 - t_1)} \qquad (10)$$

The rate ratio of leg dissociation for the minus-end site to the plus-end site is

$$\frac{k_{d-}}{k_{d+}} = \frac{\gamma_+}{\gamma_-}\left[\frac{I_{M-}(t_2) - I_{M-}(t_1)}{I_{M+}(t_2) - I_{M+}(t_1)}\right] \qquad (11)$$

which + and − mark the plus and minus ends. Similarly, the average rate for leg binding from $t_1$ to $t_2$ is

$$k_b = \frac{P(t_2) - P(t_1)}{(t_2 - t_1)} = \frac{I_M(t_1) - I_M(t_2)}{\gamma(t_2 - t_1)} \qquad (12)$$

The rate ratio of leg binding for the plus-end site to the minus-end site is

$$\frac{k_{b+}}{k_{b-}} = \frac{\gamma_-}{\gamma_+}\left[\frac{I_{M+}(t_1) - I_{M+}(t_2)}{I_{M-}(t_1) - I_{M-}(t_2)}\right] \qquad (13)$$

The leg-track binding of the present motor ensures a contact quenching of near 100% quenching efficiency (*107*) for the three dyes used, *i.e.*, $\gamma \approx 1$ and $\gamma_-/\gamma_+ \approx$

75

1 for a good approximation. Thus the probability $P(t)$ and rate ratios $k_{d-}/k_{d+}$, $k_{b+}/k_{b-}$ can be extracted directly from $I_M(t)$. The control-calibrated fluorescence also removes any influence of photobleaching.

## 4.5 Results and discussions

### 4.5.1 Motor-track formation

The motor and tracks with two or three binding sites were assembled from the DNA strands. The gel analysis of the annealed products yields one prominent band that is identified as the assembled motor or tracks (Figure 31).
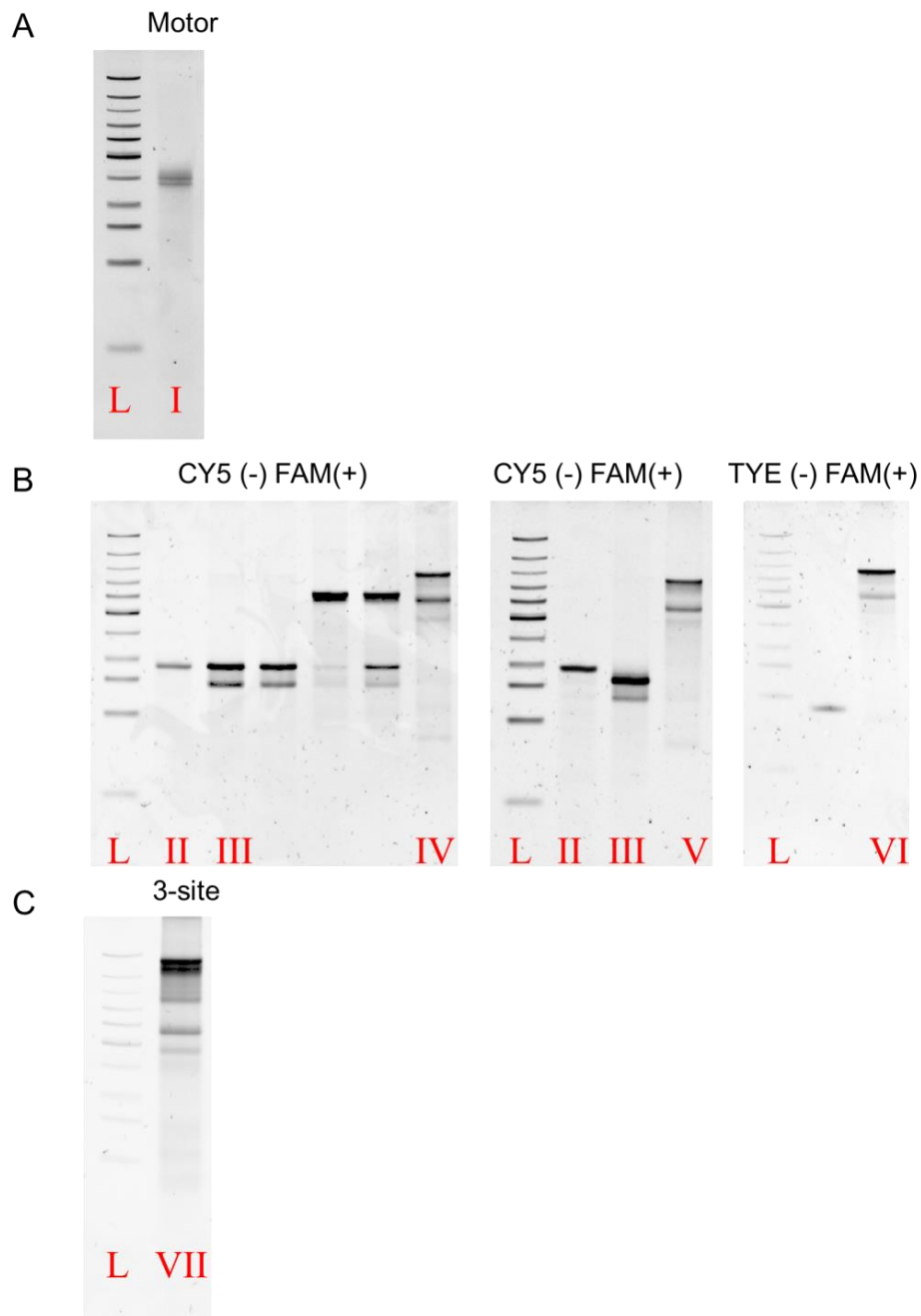
**Figure 31 The second version motor and track fabrication.** Shown are gel images obtained using native PAGE. Lanes L are the DNA ladders and panels A to C are the annealed products for the motor, three two-site tracks and three-site track, respectively. Lanes II and III show stepwise assembly of a truncated two-site track (Lane II is truncated template; III is the annealed product of the template with the 55 nt spacer strand). Lanes IV, V and VI are the full two-site tracks that have the two dyes as indicated (− and + denote minus end and plus end, respectively.) Lane VII is the annealed 3-site track.

### 4.5.2 Plus-end directed motion of the motor

Figure 32A shows the control-calibrated fluorescence signal of the motor operating on a three-site track for six visible-UV irradiation cycles. The fluorescence from the plus and minus ends drops and rises, respectively, signifying a net transfer of the motor's population from the minus end to the plus end. It is expected that the drop amount of the fluorescence signal at the plus end is less than the amount of increase at the minus end because the directionality is not perfect as some motors will bind backward and some will remain as single binding site. Panel B shows the increasing occupation probability at the plus end and the decreasing probability at the minus end. The occupation probability change averaged over the plus, minus and middle sites decreases with the operation cycles and flattens at a low value (about -5%) (panel C), suggesting that the motor mostly remains on the track during the operation-induced motion. The average occupation decrease is not caused by the entire derailment of the motor off track but by the operation-induced transition from two-leg binding states to single-leg states, because the operation cannot further derail the motor from a single-leg state due to the engine-leg separation. The rate of motion (gradient of each line segments in panel B) becomes progressively slower because the motor population at the minus end, which is available to move the plus end, becomes less after more operation cycles.
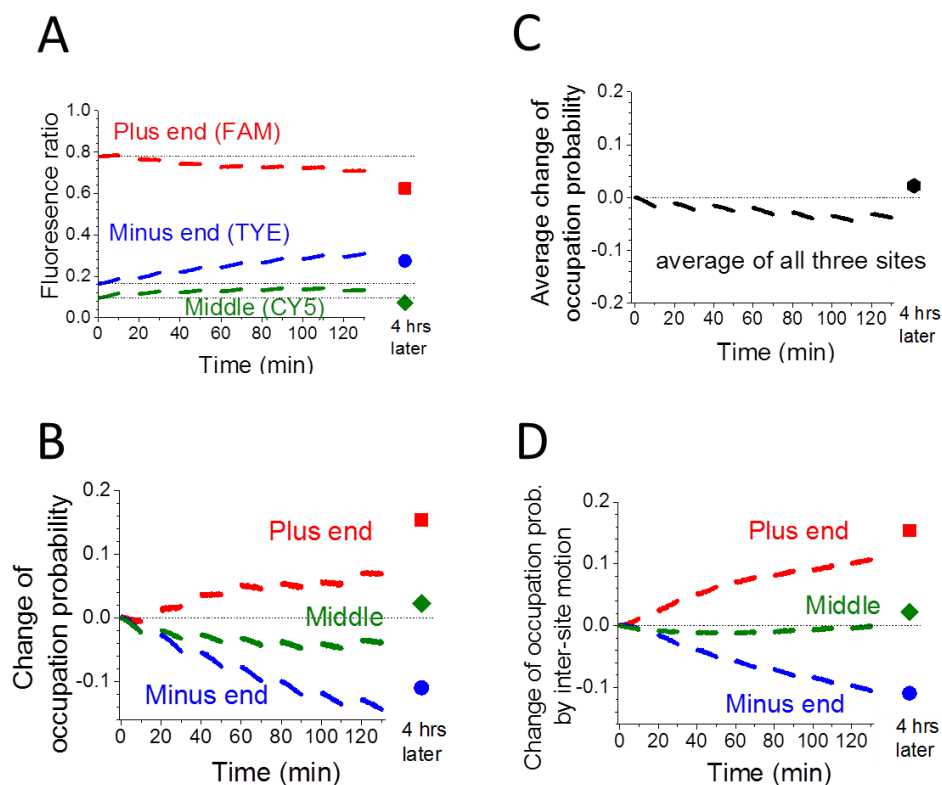
**Figure 32 Plus-end directed motility of the motor along a three-site track.**
A. Fluorescence from an equimolar mix of motor-track sample under six cycles of alternating visible light and UV irradiations (10 minutes per irradiation). Shown is the fluorescence signal calibrated against a bare-track control experiment for the same operation. The blank intervals are the time of UV irradiations when no fluorescence is collected. B–D. The change of occupation probability for the three binding sites of the track extracted from the fluorescence in A. The symbols are the data obtained after a four-hour incubation of the operated sample. The occupation change directly attributed to the motor's inter-site motion is shown in panel D, which is obtained by subtracting the data in panel B by those in panel C.

The about 5% average decrease of occupation probability is recovered by a four-hour incubation of the sample after the six-cycle operation. The recovery occurs for all the three sites as their fluorescence all drops over the post-operation incubation (panel A). This post-operation recovery is largely due to an incubation-induced recovery of the trans-cis ratio of the azobenzene moieties back to the pre-operation, equilibrated value. Since the directional transfer of the motor's population should be evaluated against the equilibrated

79

motor-track sample before the operation, the fluorescence signals immediately after the operation underestimate the motor's plus-end accumulation and overestimate the minus-end reduction (panel B). The real occupation change at each site caused by the motor's inter-site motion is obtained by subtracting the average change during the operation. The results better match the post-incubation signals, which show more than 10% occupation increase and decrease at the plus and minus ends, and a near-zero change at the middle site (panel D).

### 4.5.3  Directional preference for leg binding and dissociation

The motor's leg binding is induced by a UV irradiation that drives a transition from a single-leg state to a two-leg state. For the motor's operation on the three-site track, the fluorescence signals before and after a UV irradiation from the plus and minus ends yield the rate ratio for forward and backward binding of the dissociated leg of the single-leg state at the middle site. The rate ratio extraction is free of any complication from the single-leg states at the plus-end and minus-end sites as the leg binding from both states affects only the fluorescence from the middle site. The extracted ratio indicates a higher rate for forward binding than backward binding for all the six irradiation cycles (Figure 33A). The preference for the forward binding decreases with consecutive cycles; the same trend was previously observed for another bipedal DNA motor (*31*).
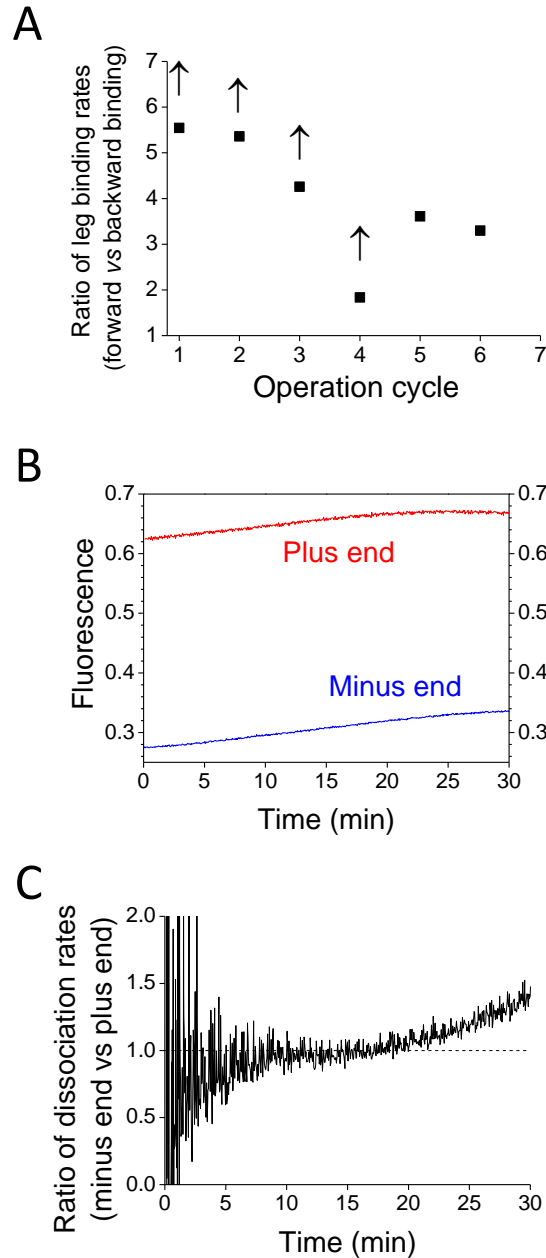
**Figure 33 Directional biases of the motor on the three-site track.** A. Rate ratio for UV-induced leg binding of the plus-end site to the minus-end site from the operation experiment of Figure 32. The shown ratio per cycle is for the average binding rates during a cycle's UV irradiation, which are estimated from the control-calibrated fluorescence data immediately before and after the UV irradiation. Since the fluorescence drop from the minus-end dye is near zero for the first four cycles (see the data in Figure 32A), this would yield an infinite ratio. We instead use the average of the larger fluorescence drop of the other two cycles to estimate a lower ratio limit for the first four cycles (indicated by upward arrows). B. The control-calibrated fluorescence signal over a single elongated visible light irradiation (30 minutes, done four hours after the six-cycle operation experiment of Figure 32). C. Rate ratio for leg dissociation of the minus-end site to the plus-end site estimated from the data in panel B. The shown ratio is for the average dissociation rates from the start of the visible irradiation to a later time as indicated by the time axis.

The motor's leg dissociation is induced by a visible light irradiation that drives a transition from a two-leg state to a single-leg state. For the motor's operation on the three-site track, the fluorescence signals from the plus and minus ends collected during an elongated visible irradiation indicate a slightly higher rate for leg dissociation from the minus end than the plus end (Figure 33B,C). However, the dissociation events at the two sites are from different two-leg bounds motors on the three-site track, and only the preference of the rear or front leg of the same motor is directly relevant to the motor's operation.

To detect any leg dissociation preference for the same motor, operation experiments on truncated two-site tracks were conducted in which the dissociation events at the plus and minus end are unambiguously related to the motor's front and rear legs, respectively. A single-cycle operation of elongated visible and UV irradiations is applied to better expose any preference. The data clearly show a higher dissociation rate for the rear leg than the front leg of the motor under the same operation (Figure 34).

## 4.5.4 Dissociation and binding preferences independent of fluorescent labels

The signals for both preferences are based on the control-calibrated fluorescence that largely removes any dependence on optical properties of the used dyes. As a further confirmation, the single-cycle operation experiments are done for two different dye labelling schemes: the initial quenching is higher for the minus end than the plus end in one case (Figure 34A), but

becomes opposite in another case (panel C); yet the same preference for rear leg dissociation is observed in both cases (panel B, D). Besides, the single-cycle operation experiments in both cases show that the UV-induced decrease of the control-calibrated fluorescence signal is more for the plus end than the minus end, further confirming the preference for forward leg binding (panel A, C).
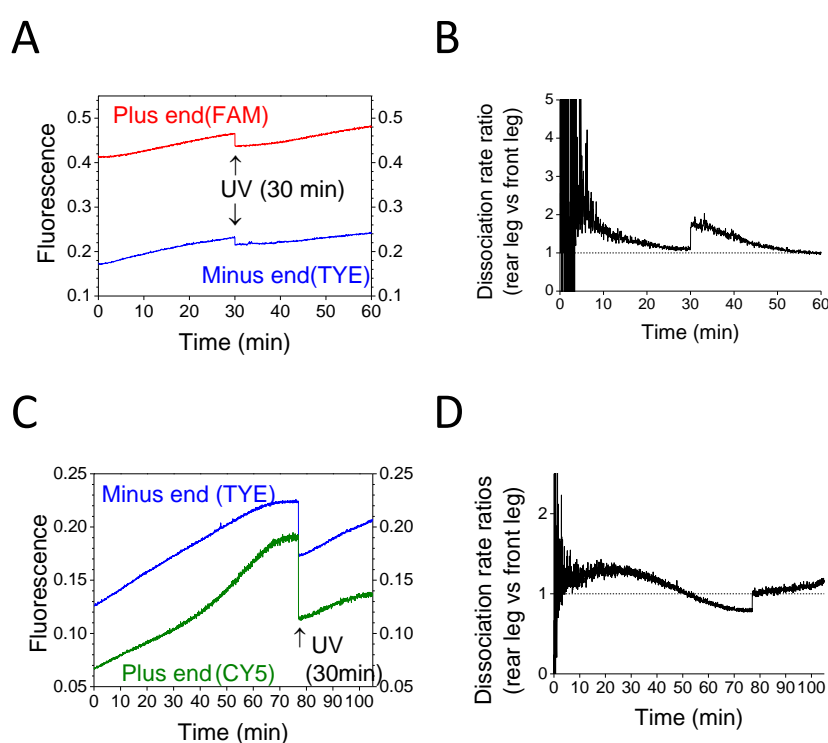


**Figure 34 Directional biases of the motor on truncated two-site tracks under an elongated single-cycle operation.** A. Control-calibrated fluorescence signal for a two-site track labelled with dyes FAM and TYE. The operation is a 30-minute visible light irradiation plus a 30-minute UV irradiation. The fluorescence was collected before and after the UV irradiation. B. Dissociation rate ratio estimated from the fluorescence data in panel A. The shown ratio is for the average dissociation rates from the start of the operation to a later time as indicated by the time axis. C, D. The same as panels A, B but for different dye labelling (CY5, TYE) and a longer visible light irradiation (77 minutes).

### 4.5.5 Dependence on light operation

A completely parameter-free comparison of the motor's performance for different durations of the visible and UV irradiations may be done for a track labelled with multiple dyes using the percentage change of control-calibrated fluorescence signals against the initial pre-operation signals of the equilibrated motor-track mix.
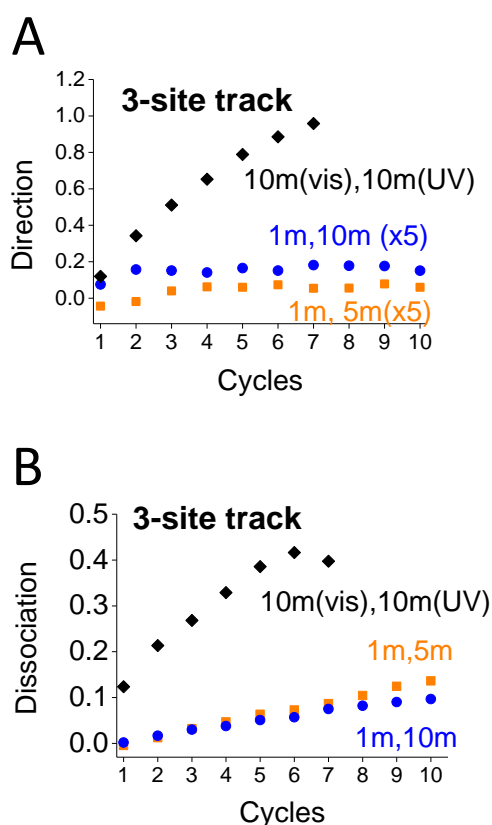


**Figure 35 Motor performance versus varied irradiation duration for three-site track.** The direction and dissociation signals are obtained from the percentage fluorescence change of the track-tethered dyes against their pre-operation fluorescence (*i.e.*, $\Delta I_M/I_{M0} = (I_M - I_{M0})/I_{M0}$, with $I_{M0}$, $I_M$ being a dye's fluorescence at the start of an operation experiment and immediately after a visible-UV irradiation cycle. Both fluorescent signals were calibrated against the bare-track control). The direction signal is the percentage change of the minus-end dye minus that of the plus-end dye; the dissociation signal is the average of the percentage changes for all the dyes on the track.
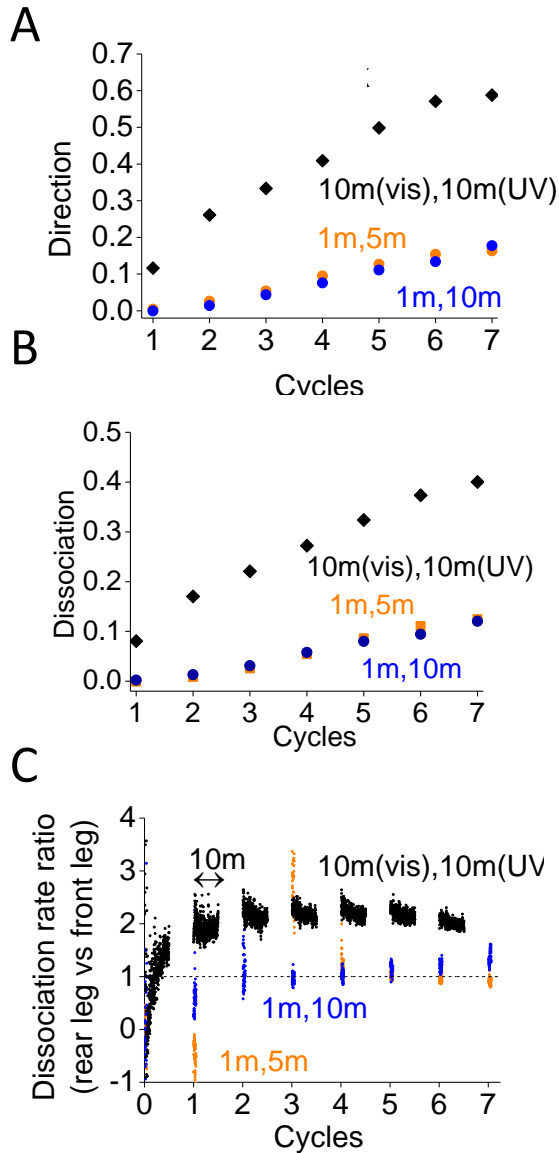
**Figure 36 Motor performance versus varied irradiation duration for 2-site track.** A, B. The direction signal and dissociation obtained in the same way as the 3-site track. C. The dissociation rate ratio is estimated in the same way as Figure 34 but for a two-site track labelled with dyes CY5 and FAM at the minus and plus ends, respectively.

The percentage change of the minus-end dye minus that of the plus-end dye reflects the motor's directional inter-site motion, and the average of percentage change over all dyes on the track reflects leg dissociation. The direction and dissociation signals thus defined are obtained for both three-site and two-site tracks under different irradiation durations (Figure 35 and Figure

36). The signals are not the absolute magnitude of the motor's direction and leg dissociation, but reflect the motor's relative performance under different operation. The results show that the motor's direction and leg dissociation signals are both reduced drastically when the irradiation cycle is shortened from 10-minute visible light and 10-minute UV to 1-minute visible light, and further to 5-minute UV. Besides, the preference for rear leg dissociation is observed again for a third dye labelling scheme (Figure 36). The dissociation rate ratio of the rear leg to the front leg rises and then flattens under consecutive cycles of irradiations. A similar pattern was previously reported for another DNA motor (*31*).

### 4.5.6 Reversed directionality

Although the motor possesses a preference for forward leg binding and rear leg dissociation, the detailed molecular mechanisms are not clear at this stage, largely due to unknown length of an unconventional DNA structure that exists transiently under the UV irradiation. However, reverse directionality shown by the fluorescent signal of the same motor operated on a shorter track (Figure 37, 45 bp spacer instead of 55 bp) suggests that the unknown structure might be rigid and beyond the binding site period (70 bp). Under this condition, the motor most likely follows the R2 regime. The length of the motor under visible light matches the track's binding site period (60 bp for the shorter track), the opposite of the requirement for a plus-end directed motion. Further UV irradiation renders the motor to be longer than the binding site period and an expulsive mode occurs. This also suggests that the motor operation follows

the first suggested mechanism (Figure 30) to achieve forward bias, instead of branch migration.
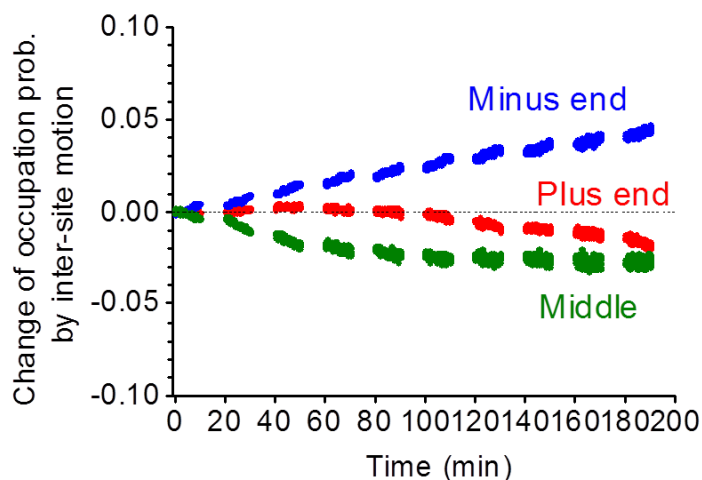


**Figure 37 Direction reversal for the motor operated on a shorter 45 bp track.** Following the same treatment in Figure 32D, the change of occupation probability directly attributed to the motor's inter-site motion is shown. The direction is reversed as the population at the minus end accumulates but reduces at the plus end.


## 4.6   Conclusion

Another modular nanomotor was demonstrated by modifying the binding legs of the first version. The control-calibrated fluorescence signal of the motor operating on a three-site track again shows a plus-end directed motion. The addition of two dyes at the start and middle of the track gives extra information regarding two key mechanisms in highly directional motor: ratchet and power stroke. The motor operation experiments on two-site tracks reaffirmed the preferential rear leg dissociation of the nanomotor. Although the preference is quantitatively weak, the effect is qualitatively clear. Moreover, the motor also possesses a preference for forward leg binding as

found for the nanomotor operating on three-site and two-site tracks. The exact mechanism for forward binding is unknown at this stage because of the unconventional structure of opened winding hairpins. Besides, a directionality reversal is observed for the same nanomotor operated at a shorter track. This matched the prediction of the design principle and gave clues on the rigidity of the unconventional structure and the forward bias mechanism.

# Chapter 5   Conclusions and outlook

## 5.1   Conclusions

A versatile modular design principle was proposed that can transform a local back-and-forth motion into processive directional movement along a linear track. As the first demonstration of principle, two light-operated DNA nanomotors were invented to implement the modular design. Both motors are symmetrical bipedal nanomotors with identical legs operating on a polar track. Following the modular design, both motors are made of two major elements: one is an engine-like bi-state component that generates force to dissociate the legs from a distance; and the other is a wheel-like binding component that is asymmetric to allow preferential dissociation along one direction of the track than the opposite direction.

Both motors achieved light-driven directional motion. Throughout the study, the same engine, a pair of light-responsive hairpins, was used to drive both motors. The first motor operates at low temperature due to its relatively short legs; the second motor achieves room-temperature operation with an elongated leg that forms more stable binding with the track. As exemplified by the two nanomotors, the design principle allows self-directed and self-propelled nanomotors to be flexibly constructed from spatially and functionally separated engine-like and wheel-like elements. This draws a close analogy to the modularized assembly of modern cars and the biological counterpart dynein. Besides, mechanistic integration of ratchet and power

stroke, which is important for high directional fidelity and efficiency, was found in one of the light-driven nanomotors.

The lack of a modular design is a major reason impeding the development of track-walking nanomotors, because a single molecular motif to perform both engine and wheel functions sets a high technical barrier. The success of the nanomotors presented shows that the modular design is a viable route for developing nanomotors from many switchable nanodevices and binding motifs from the fields of nanodevices and molecular biology. This may expand the field of nanomotors in driving methods, mechanistic sophistication and the performance to match the biological counterparts.

## 5.2   Limitations and outlook

Similar to previous reported artificial nanomotors, the motors from this study make a maximum of two steps due to the short DNA tracks. The motors have the potential to run more consecutive steps for processive operation as suggested by the data. However, this would require a rigid and longer track that is, at this stage, difficult to fabricate. Recent developments such as DNA origami and carbon nanotube (*50*) could be the feasible candidates for tracks.

The difficulty of determining the precise molecular mechanism lies in the complexity of azobenzene-tethered hairpins. However, the flexible modular design offers a simple solution to improve the two motors. For example, the hairpin engine may be replaced by a better known nanoswitch such as G-

quadruplex. The extended and contracted structure of G-quadruplex serves the role of engine like the winding hairpins; but the lengths are better known for the former. Besides, the G-quadruplex engine is probably a faster switch leading to a faster motor.

# Bibliography

1. N. Hirokawa, Kinesin and Dynein Superfamily Proteins and the Mechanism of Organelle Transport. *Science*. **279**, 519–526 (1998).
2. R. B. Nicklas, The Forces that Move Chromosomes in Mitosis. *Annu. Rev. Biophys. Biophys. Chem.* **17**, 431–449 (1988).
3. A. F. Huxley, R. Niedergerke, Structural Changes in Muscle During Contraction: Interference Microscopy of Living Muscle Fibres. *Nature*. **173**, 971–973 (1954).
4. H. Huxley, J. Hanson, Changes in the Cross-Striations of Muscle during Contraction and Stretch and their Structural Interpretation. *Nature*. **173**, 973–976 (1954).
5. J. Howard, in *Physics of bio-molecules and cells. Physique des biomolécules et des cellules*, F. Flyvbjerg, F. Jülicher, P. Ormos, F. David, Eds. (Springer Berlin Heidelberg, 2002; http://dx.doi.org/10.1007/3-540-45701-1_2), vol. 75 of *Les Houches - Ecole d'Ete de Physique Theorique*, pp. 69–94.
6. A. Yildiz, M. Tomishige, R. D. Vale, P. R. Selvin, Kinesin Walks Hand-Over-Hand. *Science*. **303**, 676–678 (2004).
7. M. von Delius, D. A. Leigh, Walking molecules. *Chem. Soc. Rev.* **40**, 3656 (2011).
8. R. D. Vale, R. A. Milligan, The Way Things Move: Looking Under the Hood of Molecular Motor Proteins. *Science*. **288**, 88–95 (2000).
9. J. A. Hammer, J. R. Sellers, Walking to work: roles for class V myosins as cargo transporters. *Nat. Rev. Mol. Cell Biol.* **13**, 13–26 (2012).
10. A. D. Mehta *et al.*, Myosin-V is a processive actin-based motor. *Nature*. **400**, 590–593 (1999).
11. A. Yildiz *et al.*, Myosin V Walks Hand-Over-Hand: Single Fluorophore Imaging with 1.5-nm Localization. *Science*. **300**, 2061–2065 (2003).
12. R. Mallik, B. C. Carter, S. A. Lex, S. J. King, S. P. Gross, Cytoplasmic dynein functions as a gear in response to load. *Nature*. **427**, 649–652 (2004).
13. A. J. Roberts, T. Kon, P. J. Knight, K. Sutoh, S. A. Burgess, Functions and mechanics of dynein motor proteins. *Nat. Rev. Mol. Cell Biol.* **14**, 713–726 (2013).
14. J. R. Kardon, R. D. Vale, Regulators of the cytoplasmic dynein motor. *Nat. Rev. Mol. Cell Biol.* **10**, 854–865 (2009).
15. J. Lin, K. Okada, M. Raytchev, M. C. Smith, D. Nicastro, Structural mechanism of the dynein power stroke. *Nat. Cell Biol.* **16**, 479–485 (2014).
16. W. Qiu *et al.*, Dynein achieves processive motion using both stochastic and coordinated stepping. *Nat. Struct. Mol. Biol.* **19**, 193–200 (2012).
17. J. D. Watson, F. H. C. Crick, Molecular Structure of Nucleic Acids: A Structure for Deoxyribose Nucleic Acid. *Nature*. **171**, 737–738 (1953).

18. W. B. Sherman, N. C. Seeman, A Precisely Controlled DNA Biped Walking Device. *Nano Lett.* **4**, 1203–1207 (2004).

19. J. S. Shin, N. A. Pierce, A synthetic DNA walker for molecular transport. *J Am Chem Soc*. **126**, 10834–10835 (2004).

20. D. A. Leigh, U. Lewandowska, B. Lewandowski, M. R. Wilson, (Springer Berlin Heidelberg, 2014), *Topics in Current Chemistry*, pp. 1–28.

21. G. Steinberg, M. Schliwa, Characterization of the Biophysical and Motility Properties of Kinesin from the Fungus Neurospora crassa. *J. Biol. Chem.* **271**, 7516–7521 (1996).

22. R. D. Vale *et al.*, Direct observation of single kinesin molecules moving along microtubules. *Publ. Online 04 April 1996 Doi101038380451a0*. **380**, 451–453 (1996).

23. N. J. Carter, R. A. Cross, Mechanics of the kinesin step. *Nature*. **435**, 308–312 (2005).

24. M. J. Schnitzer, S. M. Block, Kinesin hydrolyses one ATP per 8-nm step. *Nature*. **388**, 386–390 (1997).

25. P. Pierobon *et al.*, Velocity, Processivity, and Individual Steps of Single Myosin V Molecules in Live Cells. *Biophys. J.* **96**, 4268–4275 (2009).

26. K. Hirose, L. A. Amos, *Handbook of dynein* (Pan Stanford, Singapore, 2012).

27. Z. Wang, R. Hou, A. Efremov, Directional fidelity of nanoscale motors and particles is limited by the 2nd law of thermodynamics—Via a universal equality. *J. Chem. Phys.* **139**, 035105 (2013).

28. R. Hou, Z. Wang, Role of directional fidelity in multiple aspects of extreme performance of the F1-ATPase motor. *Phys. Rev. E*. **88**, 022703 (2013).

29. S. Green, J. Bath, A. Turberfield, Coordinated Chemomechanical Cycles: A Mechanism for Autonomous Molecular Motion. *Phys. Rev. Lett.* **101** (2008), doi:10.1103/PhysRevLett.101.238101.

30. J. Cheng *et al.*, Bipedal Nanowalker by Pure Physical Mechanisms. *Phys. Rev. Lett.* **109**, 238104 (2012).

31. M. Liu *et al.*, Autonomous Synergic Control of Nanomotors. *ACS Nano* (2014), doi:10.1021/nn406187u.

32. J. Rousselet, L. Salome, A. Ajdari, J. Prostt, Directional motion of brownian particles induced by a periodic asymmetric potential. *Nature*. **370**, 446–447 (1994).

33. L. P. Faucheux, L. S. Bourdieu, P. D. Kaplan, A. J. Libchaber, Optical Thermal Ratchet. *Phys. Rev. Lett.* **74**, 1504–1507 (1995).

34. H. Linke *et al.*, Experimental Tunneling Ratchets. *Science*. **286**, 2314–2317 (1999).

35. S.-H. Lee, K. Ladavac, M. Polin, D. G. Grier, Observation of Flux Reversal in a Symmetric Optical Thermal Ratchet. *Phys. Rev. Lett.* **94**, 110601 (2005).

36. Z. Wang, M. Feng, W. Zheng, D. Fan, Kinesin Is an Evolutionarily Fine-Tuned Molecular Ratchet-and-Pawl Device of Decisively Locked Direction. *Biophys. J.* **93**, 3363–3372 (2007).

37. J. Cheng, S. Sreelatha, I. Y. Loh, M. Liu, Z. Wang, A bioinspired design principle for DNA nanomotors: Mechanics-mediated symmetry breaking and experimental demonstration. *Methods*. **67**, 227–233 (2014).

38. J. V. Hernández, E. R. Kay, D. A. Leigh, A Reversible Synthetic Rotary Molecular Motor. *Science*. **306**, 1532–1537 (2004).

39. J. Howard, Protein power strokes. *Curr. Biol.* **16**, R517–R519 (2006).

40. Z. Wang, Synergic mechanism and fabrication target for bipedal nanomotors. *Proc. Natl. Acad. Sci.* **104**, 17921 –17926 (2007).

41. J. Bath, S. J. Green, K. E. Allen, A. J. Turberfield, Mechanism for a Directional, Processive, and Reversible DNA Motor. *Small*. **5**, 1513–1516 (2009).

42. T. Omabegho, R. Sha, N. C. Seeman, A Bipedal DNA Brownian Motor with Coordinated Legs. *Science*. **324**, 67–71 (2009).

43. Y. Tian, Y. He, Y. Chen, P. Yin, C. Mao, A DNAzyme That Walks Processively and Autonomously along a One-Dimensional Track. *Angew. Chem. Int. Ed.* **44**, 4355–4358 (2005).

44. M. You *et al.*, An Autonomous and Controllable Light-Driven DNA Walking Device. *Angew. Chem. Int. Ed.* **51**, 2457–2460 (2012).

45. P. Yin, H. Yan, X. G. Daniell, A. J. Turberfield, J. H. Reif, A unidirectional DNA walker that moves autonomously along a track. *Angew. Chem. Int. Ed.* **43**, 4906–4911 (2004).

46. J. Bath, S. J. Green, A. J. Turberfield, A Free-Running DNA Motor Powered by a Nicking Enzyme. *Angew. Chem.* **117**, 4432–4435 (2005).

47. R. Pei *et al.*, Behavior of Polycatalytic Assemblies in a Substrate-Displaying Matrix. *J. Am. Chem. Soc.* **128**, 12693–12699 (2006).

48. K. Lund *et al.*, Molecular robots guided by prescriptive landscapes. *Nature*. **465**, 206–210 (2010).

49. S. F. J. Wickham *et al.*, Direct observation of stepwise movement of a synthetic molecular transporter. *Nat Nano*. **6**, 166–169 (2011).

50. T.-G. Cha *et al.*, A synthetic DNA motor that transports nanoparticles along carbon nanotubes. *Nat. Nanotechnol.* **9**, 39–43 (2014).

51. S. K. Kufer, E. M. Puchner, H. Gumpp, T. Liedl, H. E. Gaub, Single-Molecule Cut-and-Paste Surface Assembly. *Science*. **319**, 594–596 (2008).

52. K. Hatch, C. Danilowicz, V. Coljee, M. Prentiss, Demonstration that the shear force required to separate short double-stranded DNA does not increase significantly with sequence length for sequences longer than 25 base pairs. *Phys. Rev. E*. **78**, 011920 (2008).

53. M. Rief, H. Clausen-Schaumann, H. E. Gaub, Sequence-dependent mechanics of single DNA molecules. *Nat. Struct. Mol. Biol.* **6**, 346–349 (1999).

54. H. Fu, S. Le, K. Muniyappa, J. Yan, Dynamics and Regulation of RecA Polymerization and De-Polymerization on Double-Stranded DNA. *PLoS ONE*. **8**, e66712 (2013).

55. P. L. Anelli, N. Spencer, J. F. Stoddart, A molecular shuttle. *J. Am. Chem. Soc.* **113**, 5131–5133 (1991).

56. R. A. Bissell, E. Córdova, A. E. Kaifer, J. F. Stoddart, A chemically and electrochemically switchable molecular shuttle. *Nature*. **369**, 133–137 (1994).

57. H. Murakami, A. Kawabuchi, K. Kotoo, M. Kunitake, N. Nakashima, A Light-Driven Molecular Shuttle Based on a Rotaxane. *J. Am. Chem. Soc.* **119**, 7605–7606 (1997).

58. A. M. Brouwer *et al.*, Photoinduction of Fast, Reversible Translational Motion in a Hydrogen-Bonded Molecular Shuttle. *Science*. **291**, 2124–2128 (2001).

59. D. S. Marlin, D. González Cabrera, D. A. Leigh, A. M. Z. Slawin, An Allosterically Regulated Molecular Shuttle. *Angew. Chem. Int. Ed.* **45**, 1385–1390 (2006).

60. M. C. Jiménez, C. Dietrich-Buchecker, J.-P. Sauvage, Towards Synthetic Molecular Muscles: Contraction and Stretching of a Linear Rotaxane Dimer. *Angew. Chem. Int. Ed.* **39**, 3284–3287 (2000).

61. T. Hugel *et al.*, Single-Molecule Optomechanical Cycle. *Science*. **296**, 1103–1106 (2002).

62. V. A. Azov, A. Schlegel, F. Diederich, Geometrically Precisely Defined Multinanometer Expansion/Contraction Motions in a Resorcin[4]arene Cavitand Based Molecular Switch. *Angew. Chem. Int. Ed.* **44**, 4635–4638 (2005).

63. Y. Liu *et al.*, Linear Artificial Molecular Muscles. *J. Am. Chem. Soc.* **127**, 9745–9759 (2005).

64. Y. Xiao *et al.*, Fluorescence Detection of Single-Nucleotide Polymorphisms with a Single, Self-Complementary, Triple-Stem DNA Probe. *Angew. Chem. Int. Ed.* **48**, 4354–4358 (2009).

65. Y. Liu, H. Chen, L. J. Kenney, J. Yan, A divalent switch drives H-NS/DNA-binding conformations between stiffening and bridging modes. *Genes Dev.* **24**, 339–344 (2010).

66. B. Yurke, A. J. Turberfield, A. P. Mills, F. C. Simmel, J. L. Neumann, A DNA-fuelled molecular machine made of DNA. *Nature*. **406**, 605–608 (2000).

67. D. Lubrich, J. Lin, J. Yan, A Contractile DNA Machine. *Angew. Chem. Int. Ed.* **47**, 7026–7028 (2008).

68. H. Yan, X. Zhang, Z. Shen, N. C. Seeman, A robust DNA mechanical device controlled by hybridization topology. *Nature*. **415**, 62–65 (2002).

69. H. Asanuma, T. Ito, T. Yoshida, X. Liang, M. Komiyama, Photoregulation of the Formation and Dissociation of a DNA Duplex by Using the cis–trans Isomerization of Azobenzene. *Angew. Chem. Int. Ed.* **38**, 2393–2395 (1999).

70. H. M. D. Bandara, S. C. Burdette, Photoisomerization in different classes of azobenzene. *Chem. Soc. Rev.* **41**, 1809–1825 (2012).

71. Y. Kamiya, H. Asanuma, Light-Driven DNA Nanomachine with a Photoresponsive Molecular Engine. *Acc. Chem. Res.* (2014), doi:10.1021/ar400308f.

72. X. Liang, T. Mochizuki, H. Asanuma, A Supra-photoswitch Involving Sandwiched DNA Base Pairs and Azobenzenes for Light-Driven Nanostructures and Nanodevices. *Small*. **5**, 1761–1768 (2009).

73. H. Kang *et al.*, Single-DNA Molecule Nanomotor Regulated by Photons. *Nano Lett.* **9**, 2690–2696 (2009).

74. H. Asanuma *et al.*, Synthesis of azobenzene-tethered DNA for reversible photo-regulation of DNA functions: hybridization and transcription. *Nat. Protoc.* **2**, 203–212 (2007).

75. S. Neidle, S. Balasubramanian, Eds., in *Quadruplex Nucleic Acids* (Royal Society of Chemistry, Cambridge, 2006), pp. 1–30.

76. G. Mayer, L. Kröck, V. Mikat, M. Engeser, A. Heckel, Light-Induced Formation of G-Quadruplex DNA Secondary Structures. *ChemBioChem.* **6**, 1966–1970 (2005).

77. P. Alberti, J.-L. Mergny, DNA duplex–quadruplex exchange as the basis for a nanomolecular machine. *Proc. Natl. Acad. Sci.* **100**, 1569–1573 (2003).

78. J. J. Li, W. Tan, A Single DNA Molecule Nanomotor. *Nano Lett.* **2**, 315–318 (2002).

79. K. Gehring, J.-L. Leroy, M. Guéron, A tetrameric DNA structure with protonated cytosine-cytosine base pairs. *Nature.* **363**, 561–565 (1993).

80. D. Liu, S. Balasubramanian, A Proton-Fuelled DNA Nanomachine. *Angew. Chem. Int. Ed.* **42**, 5734–5736 (2003).

81. J. Elbaz, Z.-G. Wang, R. Orbach, I. Willner, pH-Stimulated Concurrent Mechanical Activation of Two DNA "Tweezers". A "SET−RESET" Logic Gate System. *Nano Lett.* **9**, 4510–4514 (2009).

82. Y. Tang, B. Ge, D. Sen, H.-Z. Yu, Functional DNA switches: rational design and electrochemical signaling. *Chem. Soc. Rev.* **43**, 518–529 (2013).

83. I. N. Rujan, J. C. Meleney, P. H. Bolton, Vertebrate telomere repeat DNAs favor external loop propeller quadruplex structures in the presence of high concentrations of potassium. *Nucleic Acids Res.* **33**, 2022–2031 (2005).

84. Y. Dong, Z. Yang, D. Liu, DNA Nanotechnology Based on i-Motif Structures. *Acc. Chem. Res.* **47**, 1853–1860 (2014).

85. T. Liedl, F. C. Simmel, Switching the Conformation of a DNA Molecule with a Chemical Oscillator. *Nano Lett.* **5**, 1894–1898 (2005).

86. H. Gu, J. Chao, S.-J. Xiao, N. C. Seeman, A proximity-based programmable DNA nanoscale assembly line. *Nature.* **465**, 202–205 (2010).

87. Y. He, D. R. Liu, Autonomous multistep organic synthesis in a single isothermal solution mediated by a DNA walker. *Nat. Nanotechnol.* **5**, 778–782 (2010).

88. B. Lewandowski *et al.*, Sequence-Specific Peptide Synthesis by an Artificial Small-Molecule Machine. *Science.* **339**, 189–193 (2013).

89. P. W. K. Rothemund, Folding DNA to create nanoscale shapes and patterns. *Nature.* **440**, 297–302 (2006).

90. U. Feldkamp, H. Rauhe, W. Banzhaf, Software Tools for DNA Sequence Design. *Genet. Program. Evolvable Mach.* **4**, 153–171 (2003).

91. M. Zuker, Mfold web server for nucleic acid folding and hybridization prediction. *Nucleic Acids Res.* **31**, 3406–3415 (2003).

92. M. Zuker, P. Stiegler, Optimal computer folding of large RNA sequences using thermodynamics and auxiliary information. *Nucleic Acids Res.* **9**, 133–148 (1981).

93. J. N. Zadeh *et al.*, *J. Comput. Chem.*, in press, doi:10.1002/jcc.21596.

94. R. M. Dirks, J. S. Bois, J. M. Schaeffer, E. Winfree, N. A. Pierce, Thermodynamic Analysis of Interacting Nucleic Acid Strands. *SIAM Rev.* **49**, 65 (2007).

95. I. Muiznieks, W. Doerfler, DNA fragments with specific nucleotide sequences in their single-stranded termini exhibit unusual electrophoretic mobilities. *Nucleic Acids Res.* **26**, 1899–1905 (1998).

96. Q. Liu, W. A. Scaringe, S. S. Sommer, Discrete mobility of single-stranded DNA in non-denaturing gel electrophoresis. *Nucleic Acids Res.* **28**, 940–943 (2000).

97. N. C. Stellwagen, E. Stellwagen, Effect of the matrix on DNA electrophoretic mobility. *J. Chromatogr. A*. **1216**, 1917–1929 (2009).

98. R. Westermeier, in *Electrophoresis in Practice* (Wiley-VCH Verlag GmbH & Co. KGaA, 2004), pp. 9–43.

99. G. L. David, *Analytical Chemistry* (Sangam Books Ltd, Hyderabad; Great Britain, 2001).

100. D. A. Skoog, D. M. West, F. J. Holler, S. R. Crouch, *Fundamentals of Analytical Chemistry* (Cengage Learning, Belmont, CA, 9 edition., 2013).

101. M. Kubista, R. Sjöback, S. Eriksson, B. Albinsson, Experimental correction for the inner-filter effect in fluorescence spectra. *Analyst*. **119**, 417–419 (1994).

102. J. R. Lakowicz, *Principles of fluorescence spectroscopy* (Springer, New York, 3rd ed., 2006).

103. Y. Zhang, D. M. Crothers, High-throughput approach for detection of DNA bending and flexibility based on cyclization. *Proc. Natl. Acad. Sci.* **100**, 3161–3166 (2003).

104. X. Liang, H. Nishioka, N. Takenaka, H. Asanuma, in *DNA Computing*, A. Goel, F. C. Simmel, P. Sosík, Eds. (Springer Berlin Heidelberg, 2009), *Lecture Notes in Computer Science*, pp. 21–32.

105. Z. Wang, Bio-inspired track-walking molecular motors (Perspective). *Biointerphases*. **5**, FA63 (2010).

106. C. Bustamante, J. F. Marko, E. D. Siggia, S. Smith, Entropic elasticity of lambda-phage DNA. *Science*. **265**, 1599–1600 (1994).

107. S. A. E. Marras, F. R. Kramer, S. Tyagi, Efficiencies of fluorescence resonance energy transfer and contact-mediated quenching in oligonucleotide probes. *Nucleic Acids Res.* **30**, e122–e122 (2002).